DOES ROTOR-EQUIVALENT WIND SPEED DIFFER FROM HUB-HEIGHT WIND SPEED? OBSERVATIONS FROM COMPLEX TERRAIN DURING WFIP2

by

CAMDEN TYLER PLUNKETT

B.S., Embry-Riddle Aeronautical University, Prescott, Arizona, 2017

A thesis submitted to the

Faculty of the Graduate School of the

University of Colorado in partial fulfillment

of the requirement for the degree of

Master of Science

Department of Atmospheric and Oceanic Sciences

2024

Committee Members:

Julie K. Lundquist

David Kingsmill

John Cassano

Plunkett, Camden Tyler (M.S., Atmospheric and Oceanic Sciences)

Does hub-height wind speed differ from rotor-equivalent wind speed? Observations from complex terrain during WFIP2

Thesis directed by Professor Julie K. Lundquist

A rotor-equivalent wind speed (REWS) may provide a more accurate estimate for wind power forecasting and wind resource assessment compared to the hub-height wind speed (HHWS) that has historically been used to represent the momentum entering a wind turbine's rotor disk. Using LiDAR data from the Second Wind Forecast Improvement Project (WFIP2), which spanned October 2015 to April 2017, we examine differences between three previously proposed REWS variants (*REWS*, $REWS_D$, and $REWS_{Alt}$) and HHWS.

LiDAR-measured HHWS and REWS (method-independent) were very closely matched (R^2 of 0.994 to 0.999). A subset (16-32%) of outliers at sites within the Columbia Basin occurred below cut-in speed (3 m s^{-1}), thus limiting their importance for wind energy production. Outliers were further grouped into events based on temporal persistence. Numerous events were identified in which winds were of a sufficient magnitude for energy production. Diurnal and seasonal preference of outlier events above cut-in speed varied by site and REWS variant. Ridgetop locations exhibited less diurnal tendency while non-ridgetop locations favored nocturnal, morning, and evening events, especially during the warm-season months. The inclusion of turbulence intensity ($REWS_{Alt}$) reduced the number of outlier events at each site and altered diurnal and

seasonal tendencies. Outlier events above cut-out speed (25 m s^{-1}) were absent for non-ridgetop sites and, while not explicitly quantified, few.

The impact of REWS on annual energy production (AEP) was site- and variant-dependent. For sites within the Columbia Basin, AEP values calculated from REWS ranged from -1.1% to +7% relative to those calculated with HHWS.

CONTENTS

TABLES

FIGURES

1. Introduction

Wind power comprises a growing percentage of electricity shares in many countries; as of 2022, eight countries have more than 20% of their total electricity supplied by wind, with Denmark at 57%. Moreover, in 2022, additions to global wind capacity were over 77 GW. In the United States, wind power comprised the second largest source of electric-power capacity additions in 2022 (Wiser et al. 2023) and was roughly 10% of total energy production.

Wind turbines have continued to trend larger in size and capacity (Figure 1). The average hub height and rotor diameter of newly installed wind turbines in the United States during 2022 grew to 98.1 meters, and 131.6 meters, respectively. Moreover, the average "tip height" (the distance from the ground to the blade tip along the vertical axis of the turbine) for projects that became operational in 2022 was 164 meters, and the average tip height among proposed wind turbines in the FAA permitting process has burgeoned to 195 meters (Wiser et al. 2023).

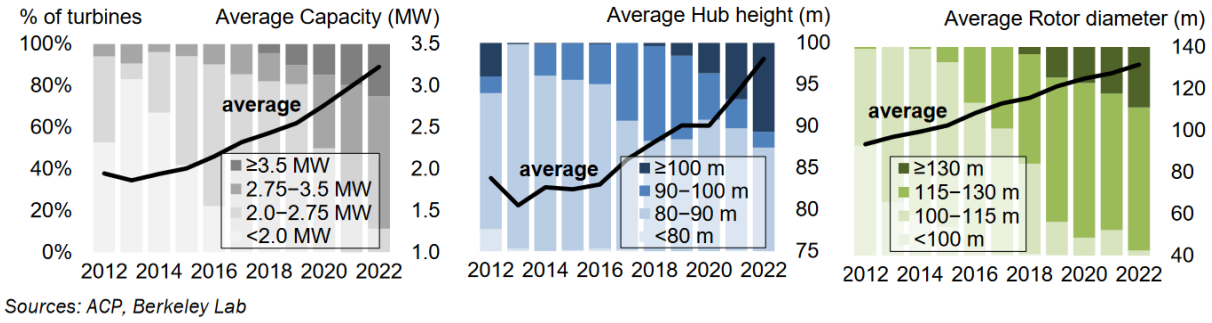

FIG. 1. Wind Turbine Trends. Figure reproduced from Wiser et al. (2023).

As interest in renewable energy continues to increase, the demand for more accurate wind forecasts increases as well. Electricity grid managers must balance supply and demand. The introduction of wind energy, which undergoes peaks and lulls due to its variable nature, complicates the task of balancing since little electricity is stored (Golston et al. 2019). One notable forecast challenge is wind ramp events, periods of steep increases or decreases in wind speed at a

given location which induce sharp up- or down-ramps in power production (Akish et al. 2019, Bossavy et al. 2013). These events can occur due to a range of weather phenomena, including synoptic-scale frontal passages, mountain waves, mix-out of cold pools, and diurnally driven gap flows. Moreover, improving rotor-layer wind speed forecasts is an active area of research (Olsen et al. 2019, Pichugina et al. 2019).

Historically, the wind speed at the height of the wind turbine's rotor hub has been used to approximate the wind speed across the entire rotor disk (Scheurich et al. 2016). While this approach often works well, as turbines continue to get larger, the potential for greater differences in wind speed and direction across the turbine's rotor disk (i.e. greater speed and directional wind shear) also increases. If the wind shear across the rotor disk is large, or if the wind profile is not smooth, significant errors in the estimation of the wind speed impacting the turbine may occur. These wind speed errors lead to increasingly large errors in the estimation of power produced by the turbine since power produced is proportional to wind speed cubed between cut-in speed and rated power (Figure 2a). Therefore, an alternative to hub-height wind speed (HHWS) is considered.

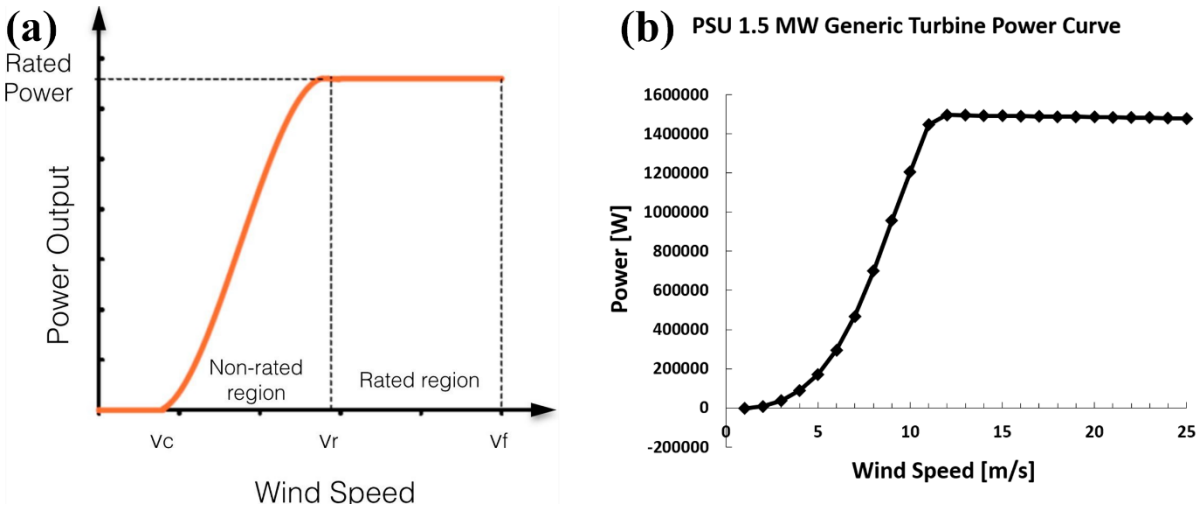

FIG. 2. Power curves reproduced from (a) Dupont et al. (2018) and (b) Pennsylvania State University's 1.5 MW generic turbine data. Cut-in (V_c), rated (V_r). and cut-out V_f) are labeled on the power curve from Dupont et al. 2018.

The alternative to HHWS is a rotor-equivalent wind speed (REWS). This REWS quantifies the momentum entering the wind turbine rotor disk by averaging the weighted wind speed over the disk's swept area. REWS theoretically offers a more accurate wind speed estimate for power production than simply using the HHWS. In regions of complex terrain, the REWS could provide a more accurate wind resource assessment, but the cost of deploying measurements that span the turbine rotor (rather than just measuring at hub height) must also be considered.

Modeling studies have been performed that incorporate REWS and quantify the difference between it and HHWS. Redfern et al. (2019) used the Weather Research and Forecasting (WRF) Model and found the difference between HHWS and REWS to be generally small, although outlier events may occur during specific meteorological events. In their 9-year, CONUS-wide modeling study, Clack et al. (2016) concluded that REWS reduces available wind power relative to HHWS. Further, they found REWS to estimate greater power production during nighttime hours and less during daytime hours relative to HHWS. They also note that wind power production estimates depend on geographic location, seasonality, and diurnal cycle.

While modeling studies offer theoretical insight into the benefits of REWS, observational studies are needed to support their findings. Scheurich et al. (2016) described an observational study in flat terrain in Northern Europe. They concluded that HHWS can be too simplistic to capture the flux of kinetic energy through the wind turbine rotor area and may over- or underestimate annual energy production (AEP). Choukulkar et al. (2016) formulated a new equation for REWS that considers both directional deviations and turbulence. Using data from two field campaigns, they noted that wind shear, directional shear, and directional fluctuations reduce wind power producing capability, while turbulent intensity increases producing capability.

In this study, the differences between three previously proposed definitions of REWS and the traditional HHWS were assessed through profiling LiDAR data collected across northern Oregon during the 18-month-long Second Wind Forecast Improvement Project (WFIP2).

This paper is organized as follows: Section 2 describes the LiDAR sites and discusses data quality and post-processing. Section 3 provides a detailed review of methods used for this study including the definitions of analyzed REWS variants, dataset outliers and outlier events, directional shear calculations, and annual energy production (AEP). Section 4 compares REWS variants to HHWS and examines outlier distributions. Section 5 offers a discussion and conclusions. Lastly, an appendix summarizes key results in plain language for the wind energy industry.

2. Data

a. LiDAR Data

To assess whether there is a difference between HHWS and REWS, data from the WFIP2 campaign was analyzed. Five sites with profiling LiDAR data collected by the University of

Colorado Boulder and Lawrence Livermore National Laboratory over the course of 18 months (October 2015 – March 2017) were chosen for this study. The utility of LiDAR data in complex terrain has been discussed, notably in Wharton et al. (2015). As shown in Figure 3, four of these sites were located across a southwest-northeast line that spanned the Columbia Basin east of the Cascade Range in Oregon, and the western-most site was located at Troutdale in the far northeastern Willamette Valley. Gordon Ridge, located just east of the Columbia River Gorge, represented the site with the highest elevation. From there, elevation decreased at the Wasco site, just east of Gordon Ridge, and continued to decrease at the Arlington site, located further east along the Columbia River. The eastern-most site was located at Vansycle Ridge in an extension of the Horse Heaven Hills near the Oregon-Washington border.

Table 1 provides site details for each of the LiDARs. In summary, Gordon Ridge and Vansycle Ridge are located along prominent ridge-top locations in the western and eastern Columbia Basin, respectively. Wasco and Arlington are lower in elevation than Gordon Ridge and Vansycle Ridge, but still above the Columbia River. Wasco is situated in a region of undulating hills south of the Columbia River, while the Arlington airport, where the LiDAR was sited, is on locally high terrain relative to the river canyon which contains the city of Arlington and is roughly 182 meters above the Columbia River at the far eastern exit to the Columbia River Gorge.

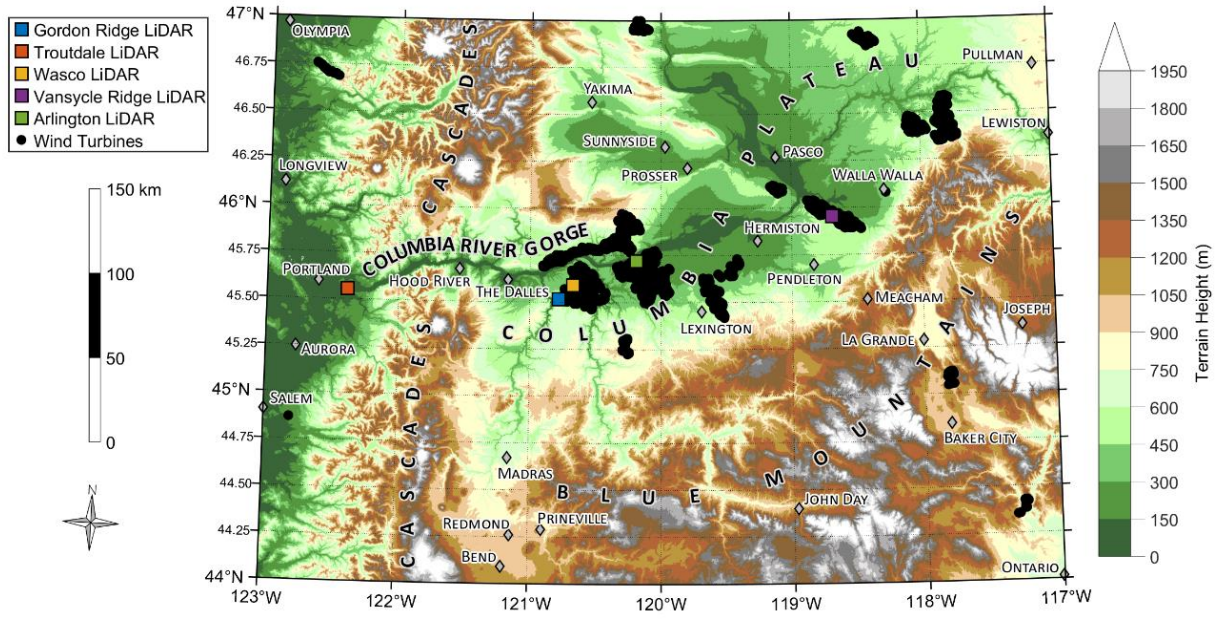

FIG. 3. Map of the WFIP2 study area containing the analyzed LiDAR data. The area, shaded by elevation, encompasses portions of northern Oregon and southern Washington. LiDAR sites are depicted by colored squares, and existing wind turbines (as of 2024) are shown in black circles where each circle represents an individual turbine. Some important geographic features are labeled.

Wind speed, wind direction, and the standard deviation of wind speed at heights of 40-220 meters above ground, in 20-meter increments, were the primary variables analyzed. Data were not available at all heights for all times during the 18-month period because each LiDAR was not in continuous operation during the period. Moreover, the ability of a LiDAR to obtain data depends on how many particulates are in the air. Cleaner air typically results in less data availability since there are fewer particles to scatter the emitted beam (Aitken et al. 2012). Data availability (Figure 3) was further impacted by weather events; fewer data were recorded during periods of active, rainy weather. The latter was especially true at the Troutdale site where it rains frequently in the winter months. Additionally, while initially deployed 20 November 2015, an instrument failure occurred at Wasco which led to lack of reliable data until its repair and redeployment on 23 February 2016. Moreover, the Troutdale LiDAR was removed on 22 February 2016, repaired, and

subsequently redeployed on 20 April 2016. As shown in Figure 5, data availability for most sampled heights was highest at Arlington where the ZephIR 300 LiDAR was sited. The Leosphere WindCube LiDARs (V1 and V2) generally exhibited lower overall data availability and more decline of availability with height. The differences in data availability may be linked to the different technologies in use; the ZephIR 300 uses continuous-wave technology (Slinger and Harris 2012), while the WindCube is a vertically profiling Doppler LiDAR (Aitken et al. 2012). Importantly, it should be noted that the entire WFIP2 campaign period (November 2015 – March 2017), plus the additional deployment period of some instruments (April 2017) was used for the calculation. Individual instruments were not in the field for the entire duration so calculated availability values would be higher if the calculations were performed for only times when the instruments were deployed. Additionally, due to time constraints for the study, only "reviewed" data from CU's LiDAR dataset (https://a2e.energy.gov/project/wfip2) were analyzed (see Analyzed Period in Table 1). Additional "raw" data are available online at which extend the dataset through early 2017 (see Deployed Period, Table 1).

TABLE 1. Site and instrument descriptions, operational and analyzed periods during the WFIP2 field.

Site	**Latitude** (decimal degrees)	**Longitude** (decimal degrees)	**Elevation** (meters above sea level)	**LiDAR Type** (unit number)	**Deployed Period**	**Analyzed Period**
Gordon Ridge	45.515620	-120.780007	728	Leosphere WindCube V2 (WC-231)	Nov 2015 – Mar 2017	Nov 2015 – Nov 2016
Troutdale	45.553418	-122.386995	12	Leosphere WindCube V1 (WC-49)	Nov 2015 – Jan 2017	Nov 2015 – Nov 2016
Wasco	45.589999	-120.672044	455	Leosphere WindCube V1 (WC-68)	Feb 2016 – Jan 2017	Feb 2016 – Nov 2016
Arlington	45.7197	-120.1874	263	ZephIR 300	Apr 2016 – Apr 2017	Apr 2016 – Apr 2017
Vansycle Ridge	45.9551	-118.6877	517	Leosphere WindCube V2	Apr 2016 – Apr 2017	Apr 2016 – Apr 2017

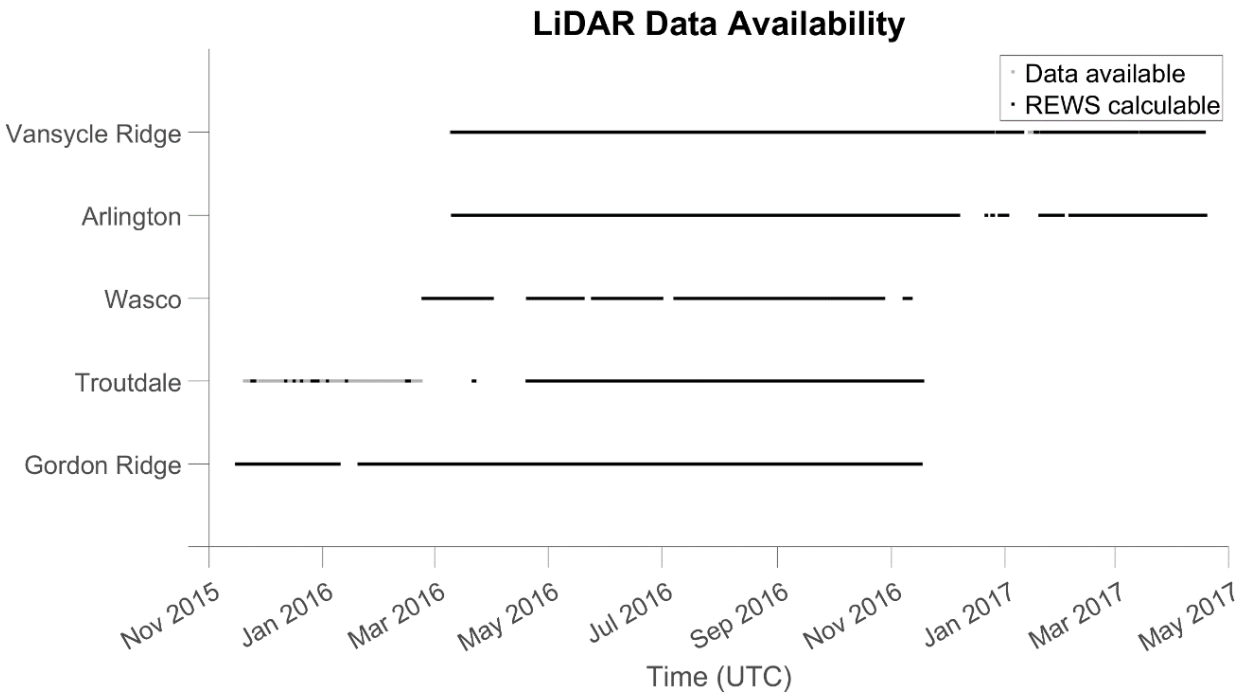

FIG. 4. LiDAR data availability of reviewed data for each site during the WFIP2 Times when at least one measurement height recorded valid data are shown with grey squares, and times where enough measurement heights were available to calculate REWS for a theoretical turbine with an 80-m hub height and 80-m rotor diameter, are shaded black.

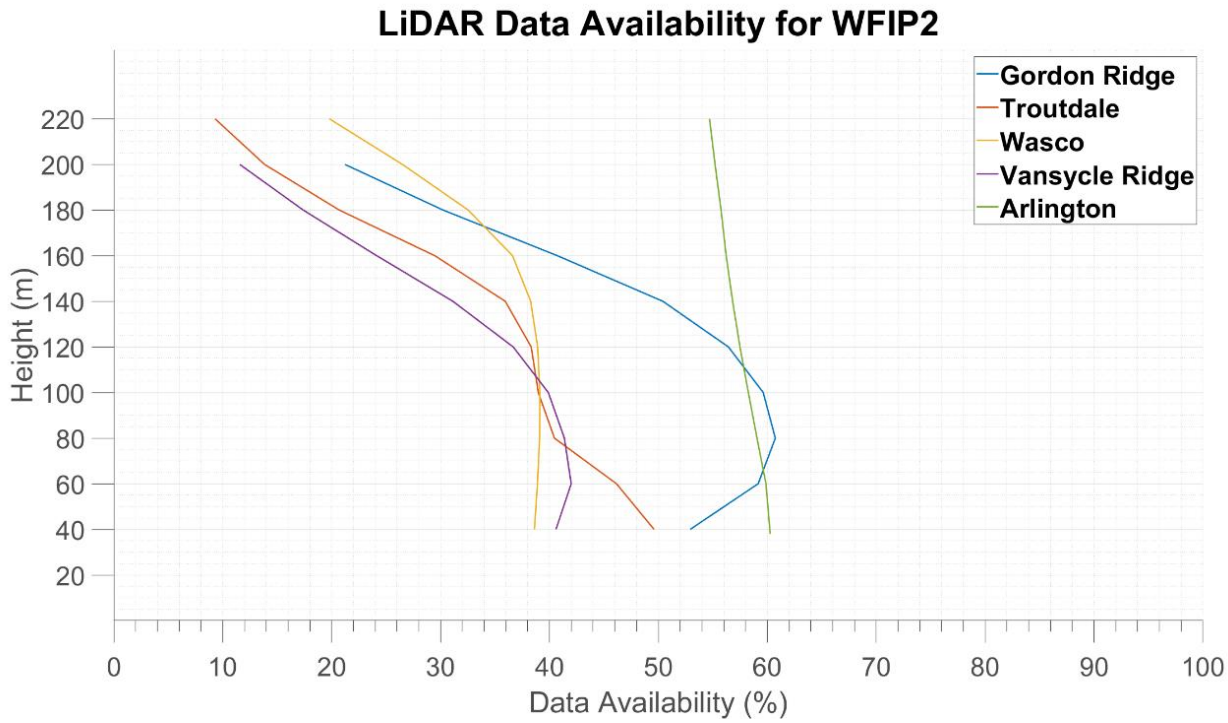

FIG. 5. LiDAR data availability at each site as a function of height for the duration of the WFIP2.

1) Data Quality and Quality Control

Basic quality control was performed on the dataset (see Bodini et al. (2019) for details) by data collectors (University of Colorado Boulder and Lawrence Livermore National Laboratory).

Upon initial analysis, wind turbine wake signatures (Iungo et al. 2013, Rhodes and Lundquist 2013) appeared in vertical profiles taken from some of the Vansycle Ridge data. Wakes in sample wind speed profiles (not shown) manifested as reduced wind speed downwind of turbines, evident at multiple measurement heights across the rotor disk, but most notable at the measurement height corresponding with hub height of turbines from the surrounding wind farms along Vansycle Ridge. Closer inspection revealed that the proximity of the LiDAR to turbines in the wind farm resulted in waking from roughly southeast directions. Thus, directions ranging from 132.7 to 201.7 degrees were subsequently removed from the Vansycle Ridge dataset per IEC standards (Vanderwende and Lundquist 2012) and excluded from further analysis.

Filtering of waked directions at Vansycle Ridge may completely or partially omit the effects of any downslope wind events that occurred during the WFIP2 campaign from being studied. Downslope wind events result in southerly to southeasterly winds that descend from above the nearby Blue Mountains, and are most prevalent in the fall, winter, and spring months (Abatzoglou et al. 2021). Typical for downslope windstorms, events are often gusty in nature; sustained winds range in magnitude from roughly 5 to 20 m s^{-1}sustained while observed gusts reach as high as 40 m s^{-1}. During these events, surface observations frequently indicate downslope winds extend along much of the foothills and northern slopes of the Blue Mountains, including at Vansycle Ridge. While not necessarily relevant to wind energy production, these winds also intersect a heavily traveled corridor, Interstate 84, in the vicinity of Cabbage Hill, Oregon east of Pendleton and are

one of the synoptic patterns that prompts the National Weather Service (NWS) Weather Forecast Office (WFO) in Pendleton to issue High Wind Warnings in the region.

To facilitate a more consistent analysis between CU and LLNL LiDAR datasets, some light post-processing was performed on the CU dataset to more closely match the LLNL dataset. Prior to post-processing, Gordon Ridge, Troutdale, and Wasco data were 2-minute averages and averaged at the end of the bin. Arlington and Vansycle Ridge data were 10-minute averages at the start and end of the bin, respectively. For this analysis, the Gordon Ridge, Troutdale, and Wasco data were converted to 10-minute averages, averaged at the end of the bin.

3. Methods

a. Rotor-Equivalent Wind Speed

While the latest IEC 61400-12-1 standard calls for the use of REWS (IEC 61400-12:2022, Van Sark et al. 2019), the literature contains many definitions which differ in complexity. Three previously proposed definitions of REWS were examined in this study to ascertain if differences among those definitions exist when applied to an observational dataset.

Power production, P, from a wind turbine is calculated by

$$P = \frac{1}{2}\rho A U^3 C_P \tag{1}$$

where ρ is air density, A is the total swept rotor area, U is the horizontal component of the wind speed, and C_P is the power coefficient (IEC 61400-12:2022). Between cut-in speed and rated speed, power production is proportional to the cube of the wind speed and sensitive to small errors in wind speed estimation (Figure 2). Above rated speed, power production is nearly constant and does not increase proportionally with the cube of the wind speed. Below cut-in speed, the turbine does not operate, thus does not produce power. Therefore, the range of wind speeds within the

region of the power curve between cut-in speed and rated speed is of most interest when examining differences between HHWS and REWS.

The first definition of rotor-equivalent wind speed (Wagner et al. 2011, Wagner et al. 2014) simply considers the weighted wind speed over the turbine's rotor disk

$$REWS = \left(\frac{1}{A}\sum_{i=1}^{N} A_i \, (\overline{U}_i)^3\right)^{1/3} \tag{2}$$

where A_i is the rotor swept area corresponding to measurement height at index i within the rotor area, $\overline{U}_i$ is the 10-minute average wind speed, and N is the number of layers (equivalent to the number of measurement heights) intersected by the rotor disk. A derivation of the rotor swept area for each layer is provided in Van Sark et al. (2019)

The second variation weights the wind speed across the turbine's rotor disk while also accounting for changes in wind direction across the disk by incorporating directional shear (IEC 61400-12:2022).

$$REWS_D = \left(\frac{1}{A}\sum_{i=1}^{N} A_i(\, \overline{U}_i cos(\theta_i - \theta_{HH}))^3\right)^{1/3} \tag{3}$$

where θ_i is the wind direction at height i and θ_{HH} is the wind direction at hub height (IEC 61400-12:2022).

The third definition is an alternate of equation (2) that accounts for turbulence of the flow. More detailed derivations of this method can be found in Wagner et al. (2009) and de Vries (1979). In short,

$$REWS_{Alt} = \left(\frac{1}{A}(\sum_{i=1}^{N} A_i \overline{U_i^{\,3}}) \right)^{1/3} \tag{4}$$

where

$$\overline{U_i^3} = \bar{U}_i^3\left(1 + 3I_i^2\right) \tag{5}$$

and

$$I_i = \frac{\sigma_i}{\bar{U}_i} \tag{6}$$

where I is the turbulence intensity and σ is the standard deviation of U at height i. This definition does not account for the vertical component of turbulence. Furthermore, the impact of turbulence on wind turbines is complex (Bardal et al. 2015, Wagner et al. 2009) and may not always realize the theoretical increase in power production that is implied by the increase in wind speed in equation 5 for non-zero horizontal turbulence intensity.

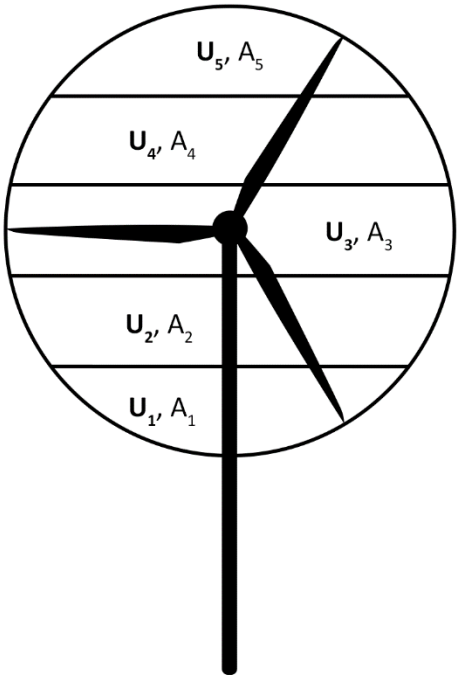

FIG. 6. Schematic showing a cross section of a wind turbine, the swept rotor area and wind speed heights used in REWS calculations. Adapted from Wagner et al. (2009).

For this study, a theoretical wind turbine with a hub height of 80 meters and a rotor diameter of 80 meters was used for the primary analysis. While a turbine of those dimensions is reasonably representative of many existing turbines in the Columbia Basin (hub heights range from 50-105 meters and rotor diameters from 47-150 meters), more recent wind farms such as the Golden Hills project just east of Gordon Ridge have seen larger turbines with hub heights of up to 105 meters and rotor diameters up to 150 meters (Hoen et al. 2018).

For each layer with area A, wind speed, wind direction, and turbulence intensity were taken to be homogeneous such that wind vector **U** was considered representative throughout the layer of depth. Ideally, an infinite number of wind vectors could be used to obtain a perfect measurement

of wind profiles, and thus an exact calculation of rotor-equivalent wind speed, but LiDAR measurements are coarser in resolution such that reasonable approximations of homogeneity must be assumed.

b. Definition of Dataset Outliers

1) TUKEY OUTLIERS

This study examines statistical outliers as determined by the Tukey method. The method was used because it is considered robust due to its use of quartiles which are inherently resistant to extreme values. Moreover, the method does not make assumptions about the analyzed distribution (Seo 2006). Tukey's method states that values which fall above Q3 + 1.5*IQR and below Q1 – 1.5*IQR, where IQR is the interquartile range (Q3 – Q1) of the distribution, are outliers. The simple difference between REWS and HHWS for each measurement time was chosen as the distribution from which to calculate outliers. The difference normalized by HHWS was considered, but upon reflection the magnitude of the difference between HHWS and REWS, rather than a normalized difference, is deemed more important due to the sensitivity of power production to differences in wind speed. The non-specific equation is given as follows:

$$Difference = HHWS - REWS \tag{7}$$

where $REWS$ is replaced with each variant of REWS such that separate difference distributions are computed for each REWS variant to determine outliers.

2) OUTLIER EVENT CLASSIFICATION

Groups of outliers were further classified into outlier events. To be classified as an event, outliers had to exhibit temporal consistency; specifically, consecutive measurements individually

classified as outliers for a duration of at least one hour were deemed collectively as an outlier "event."

c. Definition of Directional Wind Shear

Wind is a vector, containing both magnitude and direction. Wind shear can be defined as a change in wind speed and/or direction with height where pure speed shear does not consider changes in direction with height, and pure directional shear does not consider changes in speed with height. Here, similar to Sanchez Gomez and Lundquist (2019), we take the shortest rotational path between two wind vectors between measurement layers and normalize for the vertical distance between the measurement layers. Veering winds have a clockwise (positive) change with height, and backing winds have a counterclockwise (negative) change with height.

d. Annual Energy Production

Annual energy production was calculated as follows:

$$AEP = N_h \sum_{j=1}^{n} [F(U_j) P(U_j)] \tag{8}$$

where *AEP* is the annual energy production, N_h is the number of hours in one year, *n* is the number of bins, j is the bin, $F(U_j)$ is the wind frequency distribution (replaced with distributions of $HHWS$, $REWS$, $REWS_D$, and $REWS_{Alt}$), and $P(U_j)$ is the power output/curve. Moreover, from the IEC, "AEP-measured shall be obtained from the measured power curve by assuming zero power for all wind speeds above and below the range of the measured power curve" (IEC 61400-12:2022). Thus, all speeds below cut-in and above cut-out were removed for the calculation. The power curve was taken from the 1.5 MW Pennsylvania State University (PSU) generic turbine, which is based on a General Electric SLE 1.5 MW turbine with an 80-m hub height and 77-m rotor

diameter. Details are outlined by Schmitz (2011). This turbine is similar in size and power output to many existing turbines in the Columbia Basin (Hoen et al. 2018)

4. Results

a. Annual Energy Production

As shown in TABLE 3 and TABLE 4, AEP was dependent on which variant of REWS was used in the calculation. At Troutdale, HHWS overestimated AEP relative to all REWS variants, while at Arlington, HHWS underestimated AEP. For all other sites, over- or underestimation varied based on the REWS definition. Notably, $REWS_{Alt}$ provided the highest AEP of the REWS variants at all sites.

TABLE 2. Calculated AEP (MWh) for each site based on PSU's 1.5MW turbine, LiDAR-measured HHWS, and calculated REWS variants.

	Gordon Ridge	**Troutdale**	**Wasco**	**Arlington**	**Vansycle Ridge**
HHWS	$5.66x10^3$	$1.94x10^3$	$5.79x10^3$	$5.09x10^3$	$5.52x10^3$
REWS	$5.75x10^3$	$1.67x10^3$	$5.75x10^3$	$5.34x10^3$	$5.53x10^3$
$\boldsymbol{REWS_D}$	$5.70x10^3$	$1.67x10^3$	$5.73x10^3$	$5.33x10^3$	$5.53x10^3$
$\boldsymbol{REWS_{Alt}}$	$5.95x10^3$	$1.77x10^3$	$5.85x10^3$	$5.44x10^3$	$5.66x10^3$

TABLE 3. Calculated AEP (MWh) as a percent of HHWS-estimated AEP (MWh).

	Gordon Ridge	**Troutdale**	**Wasco**	**Arlington**	**Vansycle Ridge**
HHWS	100	100	100	100	100
REWS	102	86.0	99.3	105	100
$\boldsymbol{REWS_D}$	101	86.0	98.9	105	100
$\boldsymbol{REWS_{Alt}}$	105	91.2	101	107	103

b. Wind Speed and Direction Distributions during WFIP2

1) HUB-HEIGHT WINDS

The unique terrain of the Pacific Northwest influences the speed and direction distributions at all locations due to often marked differences in air mass characteristics between the west and east side of the Cascades (Sharp and Mass 2004). Gap flows through the Columbia River Gorge (a low point along the Cascade crest), easterly offshore winds, and lighter winds during wintertime cold pools in the Columbia Basin are the predominant synoptic patterns.

Distributions of wind speed and direction varied across sites, as illustrated in Figure 7 which displays wind roses of 80-m HHWS during WFIP2 for location. The influence of terrain is evident

when examining speed and direction distributions. All sites located within the Columbia Basin had a dominant westerly component while Troutdale favored an easterly direction (Figure 7b). Distributions at Wasco (Figure 7c) and Arlington (Figure 7d) were bimodal, exhibiting a dominant direction of southwesterly (Arlington) to westerly (Wasco) with a secondary maximum from the northeast (Arlington) to east (Wasco).

Winds at Gordon Ridge (Figure 7a) and Troutdale were subtly trimodal. The dominant direction at Gordon Ridge, as at Wasco and Arlington, was southwesterly to westerly, with a secondary peak from the northeast. Additionally, a tertiary peak containing some of the strongest observed winds at Gordon Ridge is evident from the south-southwest. The strongest winds at Troutdale occurred from the east to east-southeast because of both offshore easterly gap flows and cold-pool-driven easterly flow. Secondary and tertiary maxima from the west-northwest and south-southwest resulted from onshore flow and weakly forced regimes.

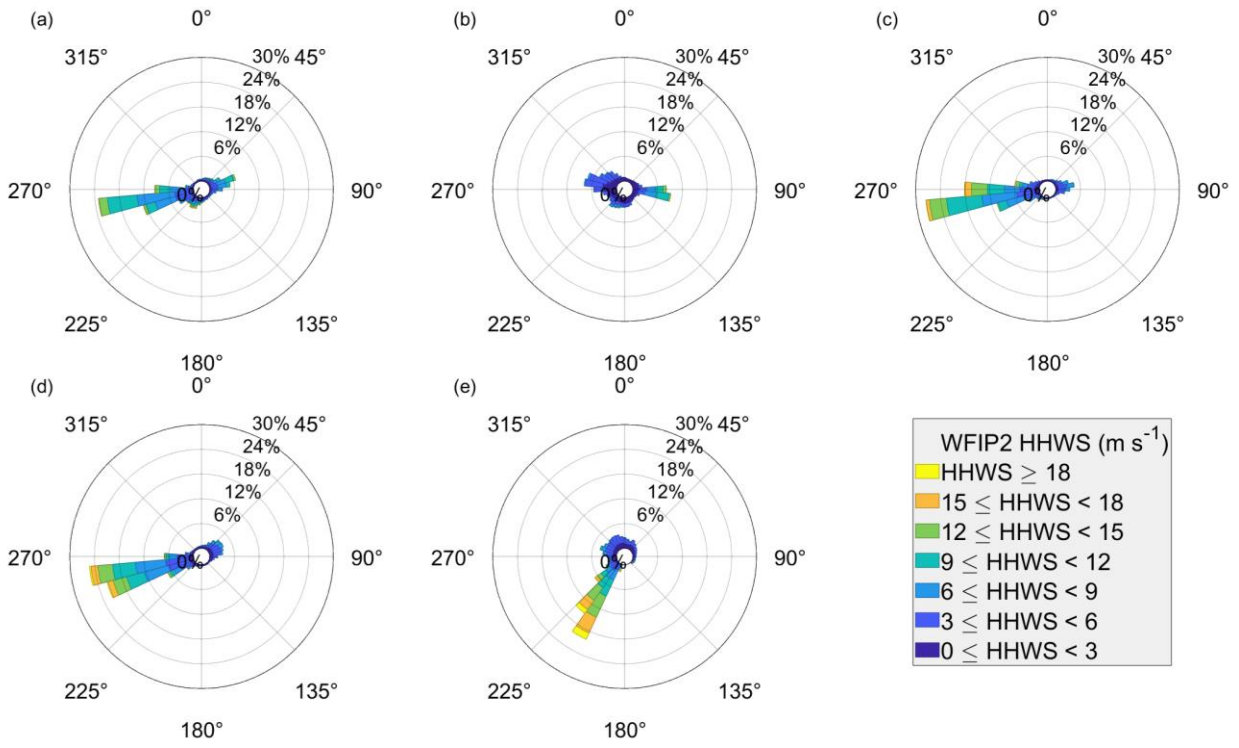

FIG. 7. 80-m HHWS during WFIP2 at (a) Gordon Ridge, (b) Troutdale, (c) Wasco, (d) Arlington, and (e) Vansycle Ridge. Waked directions have been removed at Vansycle Ridge.

Winds at Vansycle Ridge (Figure 7e) were quasi-trimodal with peaks from the south-southwest, north, and southeast. However, the removal of waked directions resulted in the quasi-bimodal distribution shown in Figure 7e. The overwhelming majority of strong winds had a southerly to southwesterly direction.

Weibull probability density functions (PDFs) are given by

$$f(U|\lambda,k) = \frac{k}{\lambda}\left(\frac{U}{\lambda}\right)^{k-1} exp\left[-\left({}^{U}/_{\lambda}\right)^{k}\right], U \geq 0, \quad (9)$$

where λ is the scale parameter and k is the shape parameter.

Weibull PDFs fit to 80-m HHWS (Figure 8) closely matched the observations at Gordon Ridge and Wasco, qualitatively. The Weibull distribution fits did not match observed data as well at Arlington and Troutdale, and the fit at Vansycle Ridge was poor. Average wind speeds were

strongest for the sites in the Columbia Basin with weaker average wind speeds at Troutdale. This is also evident in Figure 6. Furthermore, the shape parameter k (top right of each subfigure) indicated more variability at Troutdale and Vansycle Ridge than at the other sites.

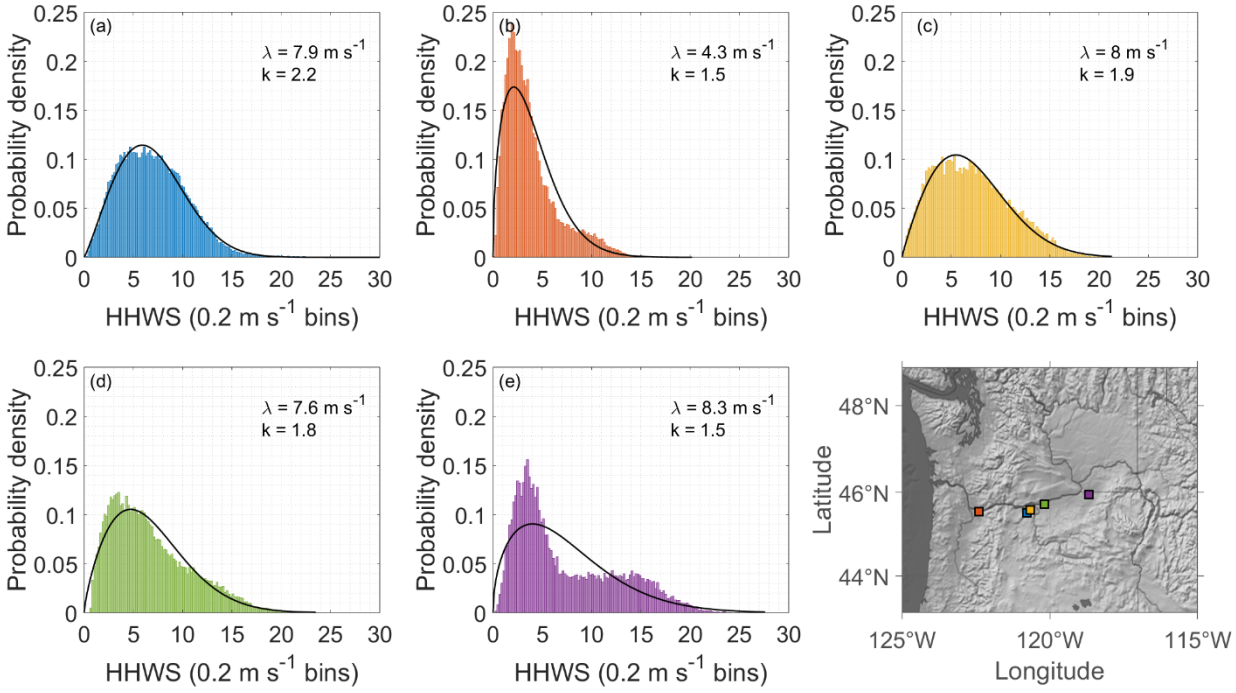

FIG. 8. Histograms of 80-m HHWS during WFIP2 at (a) Gordon Ridge, (b) Troutdale, (c) Wasco, (d) Arlington, and (e) Vansycle Ridge. Weibull probability density function fits are overlaid and associated scale λ and shape k parameters are shown in the upper right corner of each subplot.

c. Outliers

1) HUB-HEIGHT VS ROTOR-EQUIVALENT WINDS

Binned scatter plots of 80-m HHWS versus REWS variants (Figures 9, 10, and 11) show generally excellent agreement between 80-m HHWS and $REWS$, $REWS_D$, and $REWS_{Alt}$. Linear regressions and their associated R^2values are displayed on each subfigure. R^2 values ranged from 0.994 to 0.999 depending on site and REWS variant. While some visual outliers, pairs away from the 1:1 line (not shown) are apparent at each site, a large concentration of pairs fall near the 1:1 line.

Visual outliers between cut-in and rated speed are evident for all sites and REWS variants, but the percentages were not explicitly calculated.

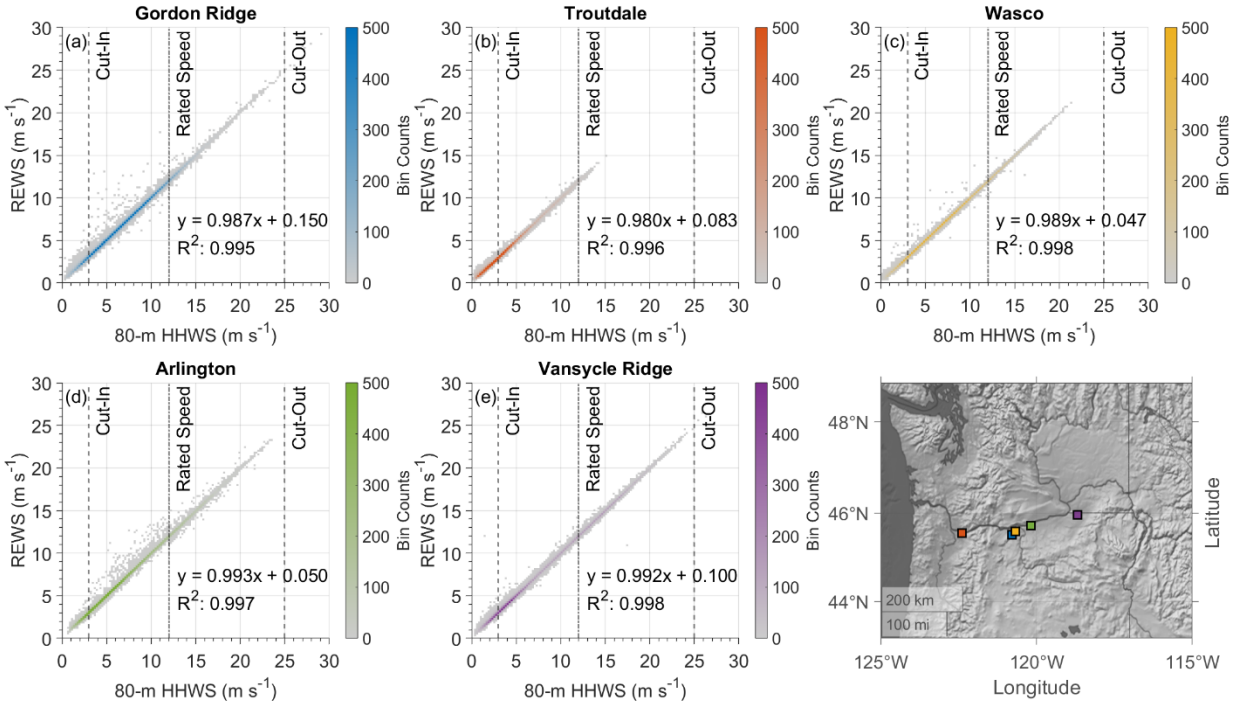

FIG. 9. Binned scatter plot of *REWS* vs 80-m HHWS during WFIP2 at (a) Gordon Ridge, (b) Troutdale, (c) Wasco, (d) Arlington, and (e) Vansycle Ridge. Linear regression equations and R^2 values are displayed in the lower right corner for each site. A site map is provided in the lower right subplot.

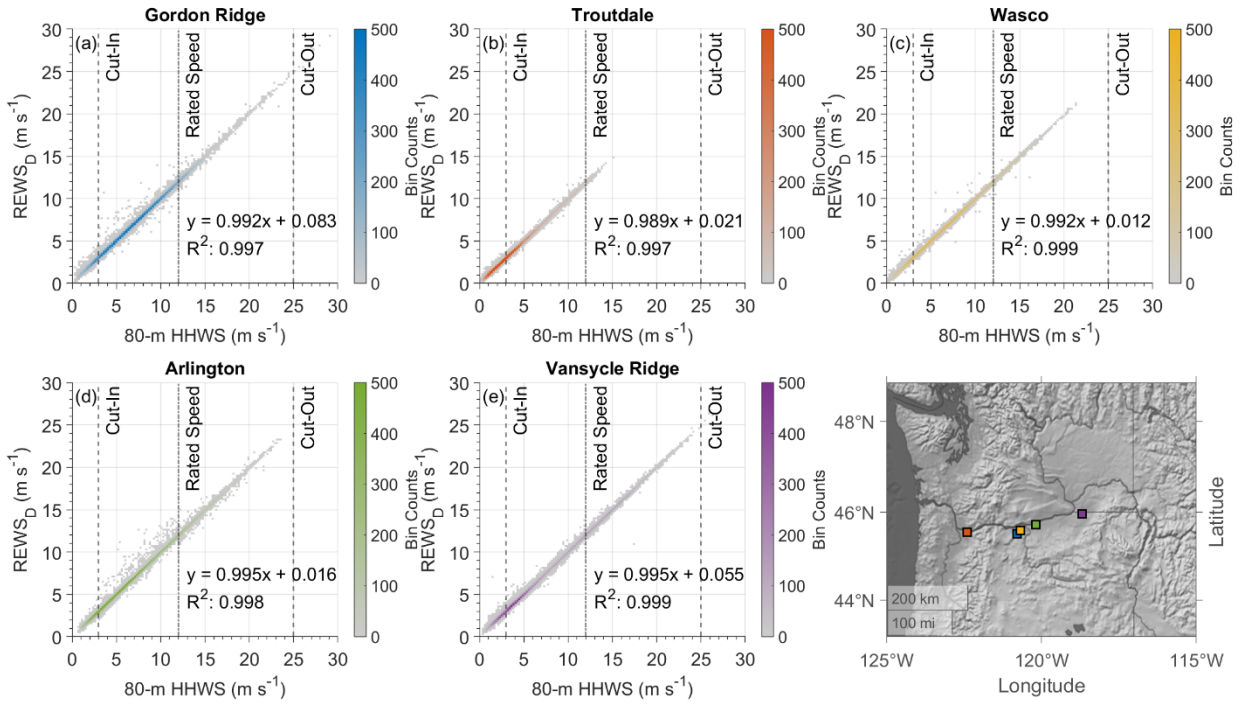

FIG. 10. Binned scatter plot of $REWS_D$ vs 80-m HHWS during WFIP2 at (a) Gordon Ridge, (b) Troutdale, (c) Wasco, (d) Arlington, and (e) Vansycle Ridge. Linear regression equations and R^2 values are displayed in the lower right corner for each site. A site map is provided in the lower right subplot.

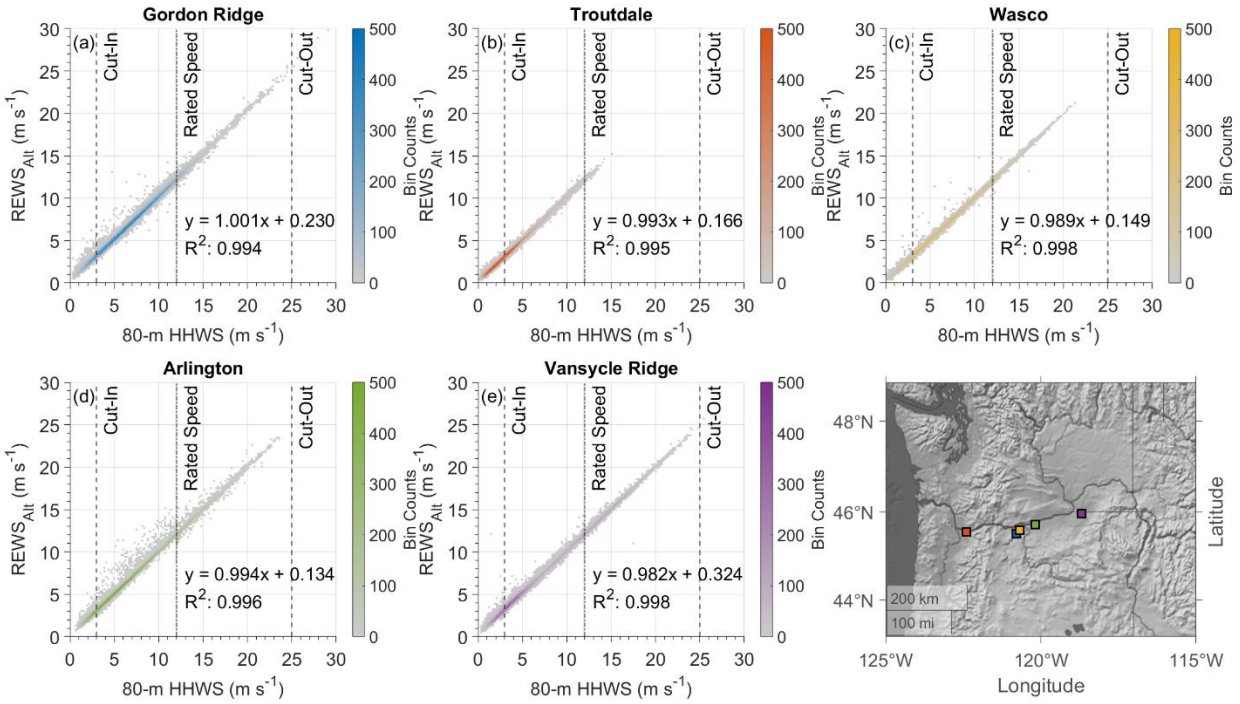

FIG. 11. Binned scatter plot of $REWS_{Alt}$ vs 80-m HHWS during WFIP2 at (a) Gordon Ridge, (b) Troutdale, (c) Wasco, (d) Arlington, and (e) Vansycle Ridge. Linear regression equations and R^2 values are displayed in the lower right corner for each site. A site map is provided in the lower right subplot.

The percentage of 80-m HHWS and REWS outliers that were below cut-in speed are given in Table 2. More than 50% of all outliers at Troutdale were below cut-in speed. The percentage of outliers below cut-in speed was considerably less at the sites in the Columbia Basin, but still ranged from 16% to 32%. Since they are below cut-in speed, these outliers can be considered unimportant for wind energy.

TABLE 4. Percentage of outlier times that HHWS was below cut-in speed during WFIP2.

Site	$\boldsymbol{REWS}$	$\boldsymbol{REWS_D}$	$\boldsymbol{REWS_{Alt}}$
Gordon Ridge	23	16	17
Troutdale	64	54	54
Wasco	31	25	31
Arlington	25	21	20
Vansycle Ridge	28	22	32

The distribution of directional wind shear varied on a site-by-site basis (Figure 12), but a slight tendency towards veering is visually evident at all sites.

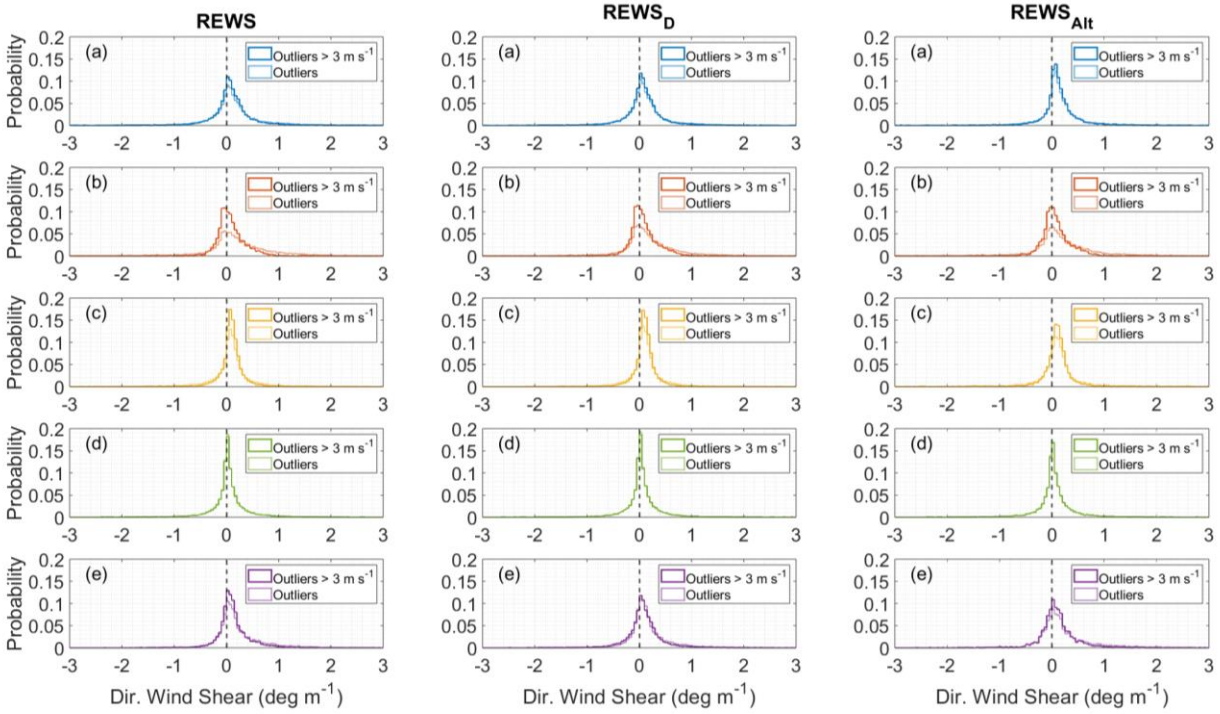

FIG. 12. Directional wind shear for each REWS variant (column) during outlier times at (a) Gordon Ridge, (b) Troutdale, (c) Wasco, (d) Arlington, and (e) Vansycle Ridge.

2) OUTLIER EVENTS DURING WFIP2

Individual outlier events defined in section 3.2 were plotted in Figures 13-15 for equations 2-4, respectively. Colors match the site colors on the map (Figure 1) and data were filtered to show

events above cut-in speed. For events with less than six consecutive times (equivalent to one hour in duration) displayed in the figure, some of the data were below cut-in speed and filtered from the figure. Thus, if an event had both data below and above cut-in speed, only the values above cut-in speed were shown.

Events as calculated from $REWS$, $REWS_D$, and $REWS_{Alt}$ were scattered diurnally and seasonally throughout the WFIP2 campaign. The varying analysis and deployment periods for each LiDAR are evident and while Figures 13 through 15 offer insight into individual events during the field campaign, they do not fully elucidate the diurnal and seasonal tendencies of outlier events.

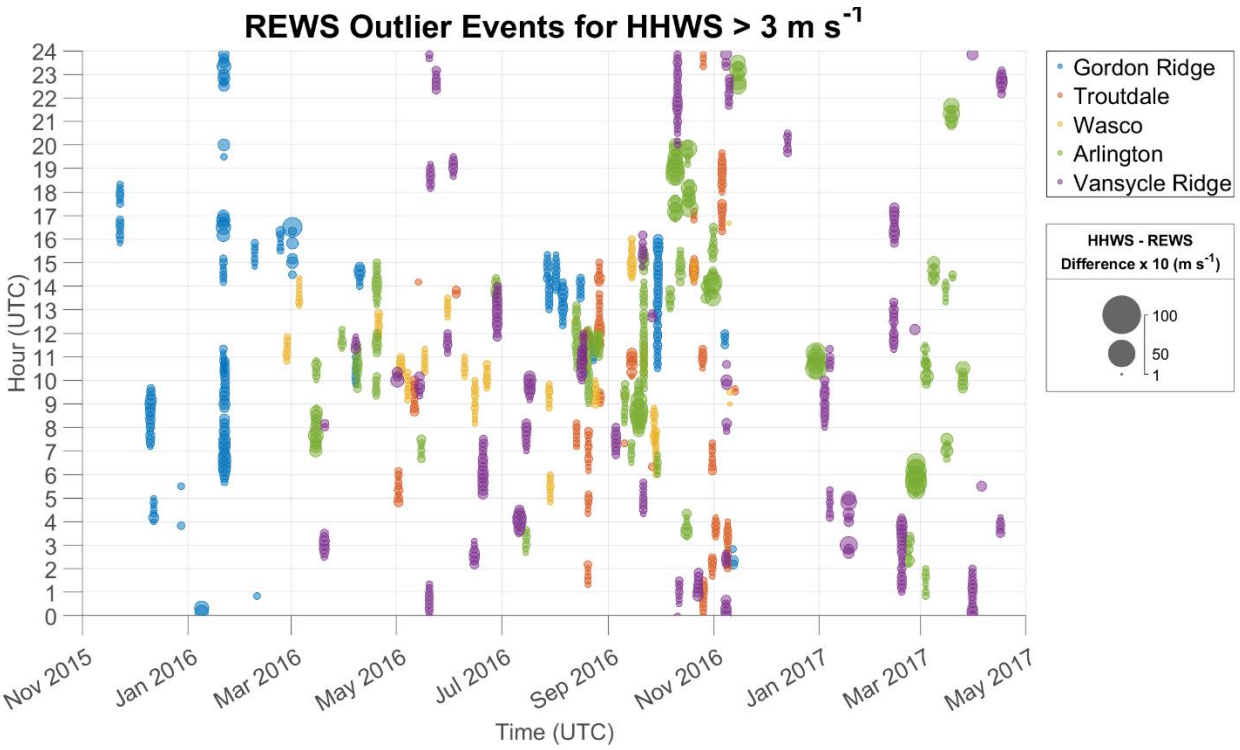

FIG. 13. Outlier event times during WFIP2 based on *REWS* for times when 80-m HHWS was greater than cut-in speed. Outlier times are represented by bubbles, scaled by the magnitude of the difference between 80-m HHWS and *REWS* at that time. Larger bubbles indicate a larger difference between 80-m HHWS and *REWS*. Events are color coded by site. Times are in UTC.

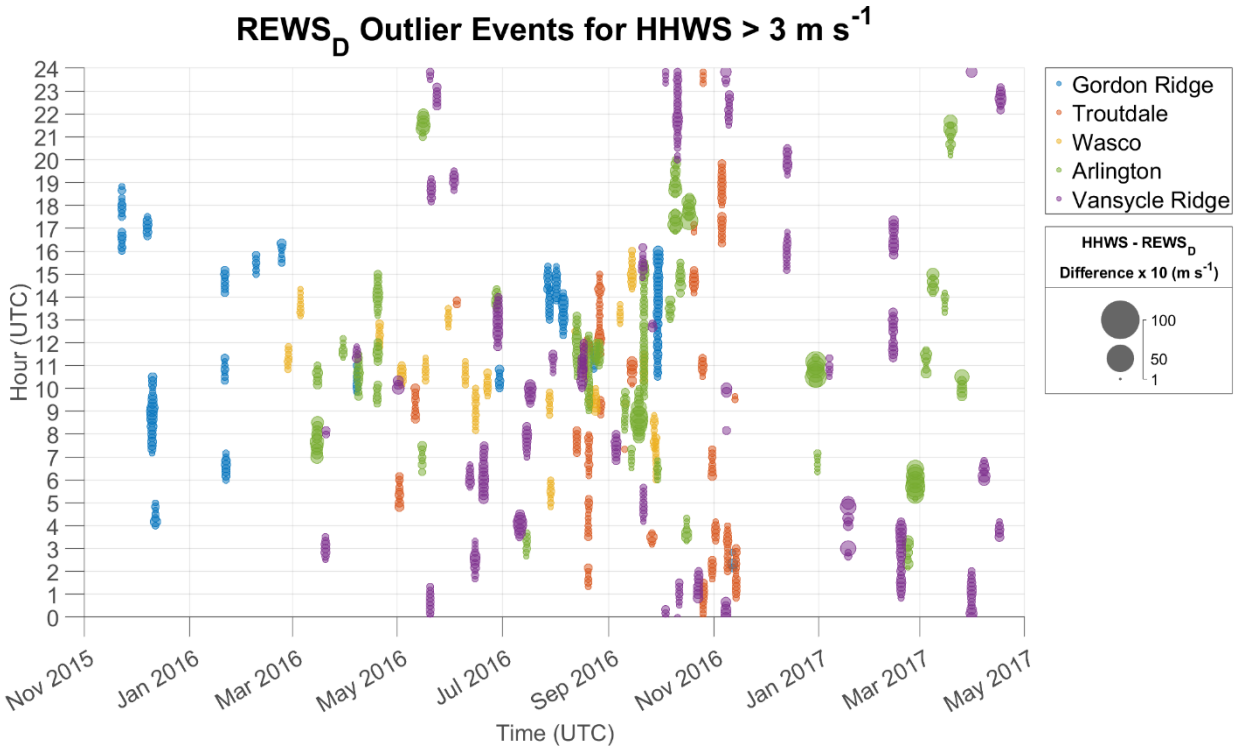

FIG. 14. Outlier event times during WFIP2 based on $REWS_D$ for times when 80-m HHWS was greater than cut-in speed. Outlier times are represented by bubbles, scaled by the magnitude of the difference between 80-m HHWS and $REWS_D$ at that time where larger bubbles indicate a larger difference between 80-m HHWS and $REWS_D$. Events are color coded by site. Times are in UTC.

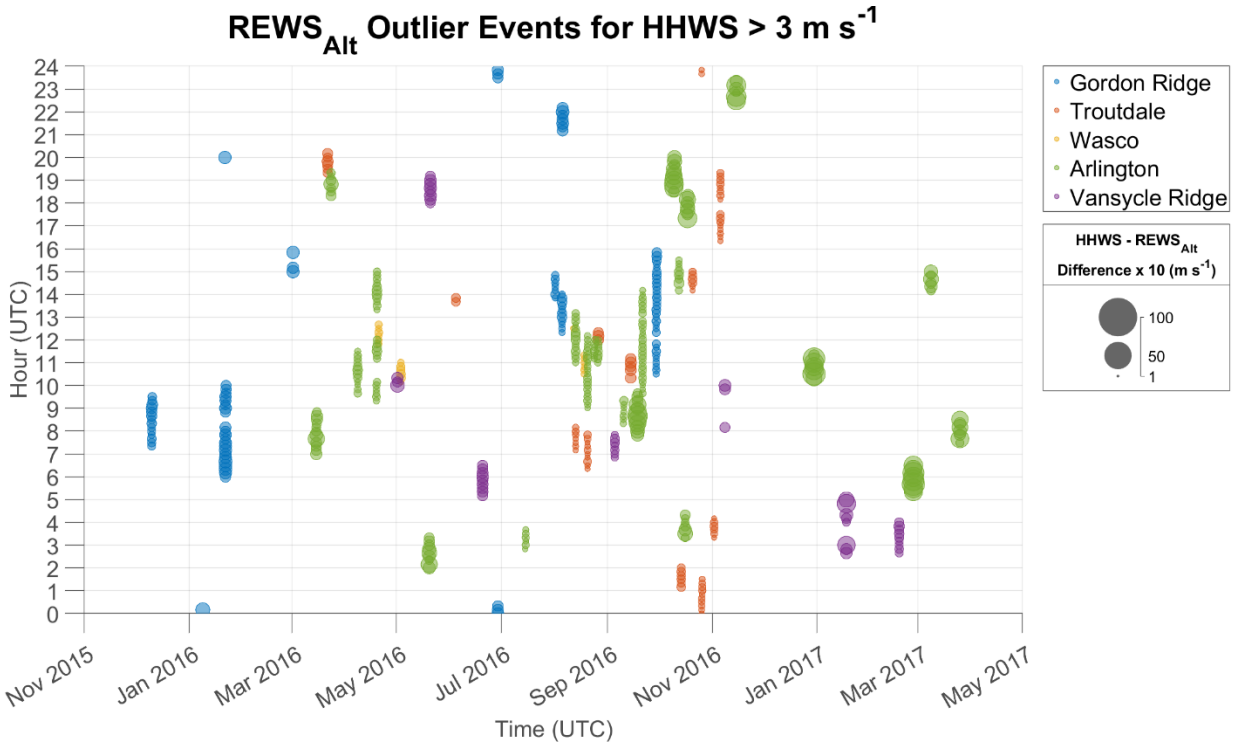

FIG. 15. Outlier event times during WFIP2 based on $REWS_{Alt}$ for times when 80-m HHWS was greater than cut-in speed. Outlier times are represented by bubbles, scaled by the magnitude of the difference between 80-m HHWS and $REWS_{Alt}$ at that time where larger bubbles indicate a larger difference between 80-m HHWS and $REWS_{Alt}$. Events are color coded by site. Times are in UTC.

To account for the varying deployment periods and data availability, data were normalized by data availability for each hour and month at each site. The resulting joint probabilities were organized into heatmaps to facilitate analysis of diurnal and seasonal tendencies. When qualitatively examining these heatmaps (Figure 16) of REWS outliers above cut-in speed, it is immediately apparent that outliers occurred at varying times throughout the day and year depending on the site and REWS variant. $REWS$ and $REWS_D$ outliers at Wasco and Arlington exhibited a notable preference for the evening transition period, nighttime, and morning transition period. Vansycle Ridge and Gordon Ridge, showed less of a diurnal preference. $REWS_{Alt}$ outliers show a reduction in frequency of events, except at Gordon Ridge during the afternoon and evening hours.

In general, all sites showed a less coherent diurnal pattern during spring, fall, and winter, seasons in which there are more frequent passing low-pressure systems and stronger synoptic forcing which may disrupt the formation of the nocturnal stable boundary layer. The synoptic pattern over the Pacific Northwest in the summer months, especially July and August, is characterized by dominant upper-level ridges of high pressure. While there are infrequent passing low-pressure systems, and other synoptic-scale events such as marine pushes (surges of marine air from west of the Cascades through the Cascade gaps to the east side), the nocturnal stable boundary layer is more likely to consistently form in the absence of strong synoptic forcing.

The relative lack of preference at Gordon Ridge and Vansycle Ridge was likely due to their more exposed ridgetop locations. In contrast, Wasco and Arlington were sited in relatively sheltered locations when compared to the ridgetop sites.

While it is a less important location for wind energy production, Troutdale, at the western exit of the Columbia River Gorge had far fewer outliers above cut-in speed compared to the sites east of the Cascades.

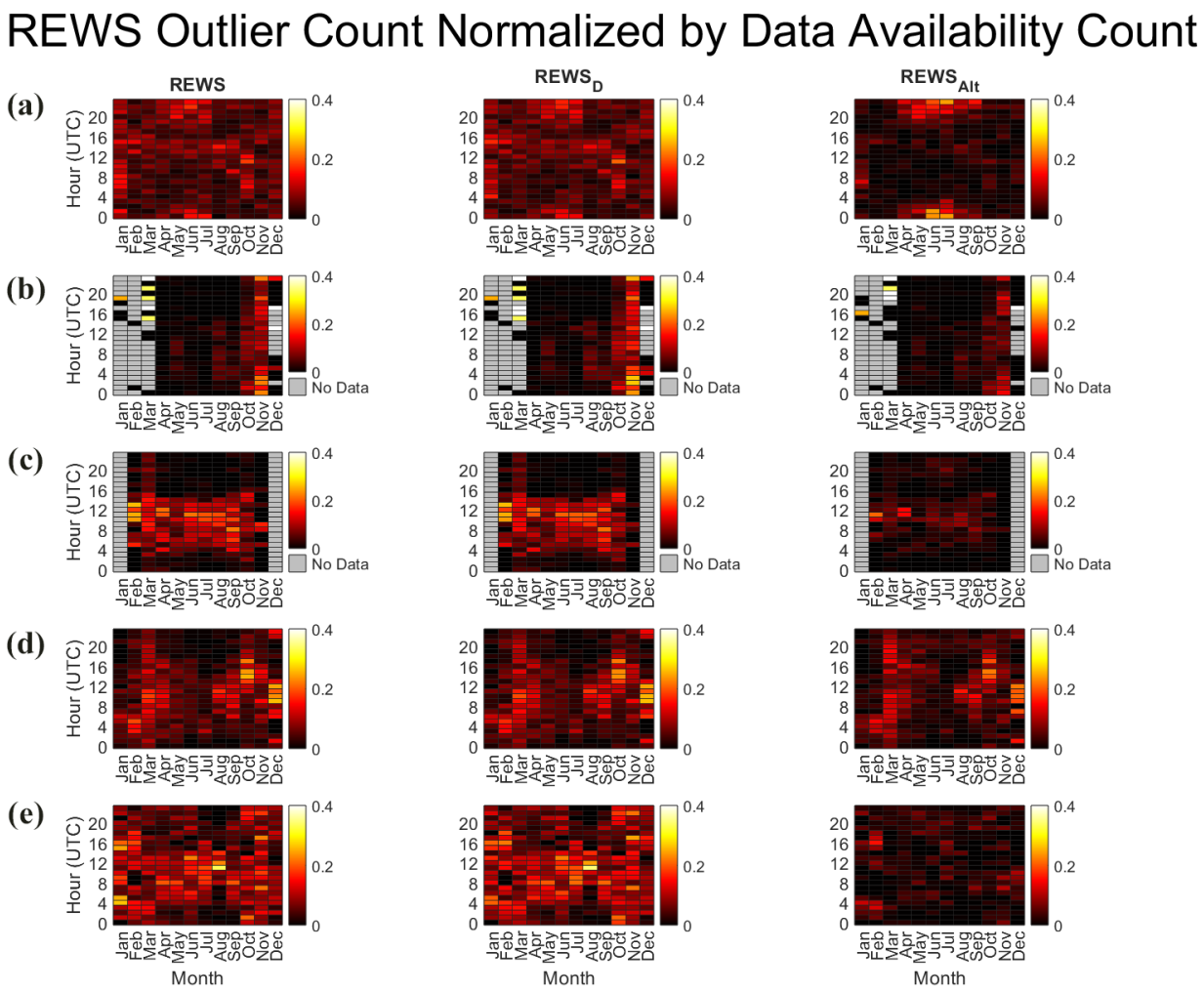

FIG. 16. Heatmap of outlier event times during WFIP2 for 80-m HHWS above cut-in speed, normalized by data availability count for each hour and month bin. Times are in UTC. Rows from top to bottom represent (a) Gordon Ridge, (b) Troutdale, (c) Wasco, (d) Arlington, and (e) Vansycle Ridge.

3) HUB-HEIGHT WINDS DURING OUTLIER EVENTS

Hub-height winds, filtered to exclude speeds below cut-in speed, are provided in Figures 17, 18, and 19 for $REWS$, $REWS_D$, and $REWS_{Alt}$ outlier events, respectively. $REWS$ and $REWS_D$ outlier wind roses at Gordon Ridge, Wasco, Arlington, and Vansycle Ridge exhibited similar distributions regarding outlier directions when compared with their overall distributions from WFIP2, but Troutdale showed significant differences in directions. At Troutdale, easterly and south-southeasterly winds were the most frequently observed outlier directions while very few

outliers were from the southwest or northwest. At Vansycle Ridge, outliers were comprised of more northwesterly and southeasterly wind directions relative to its WFIP2 distribution. Outliers from the east, north, or northeast were weaker in magnitude at Gordon Ridge, Wasco, Arlington, and Vansycle Ridge compared to those with a westerly component. From a synoptic standpoint, this is expected since synoptic-scale pressure gradients across the Columbia Basin are typically much weaker during cold pools or easterly wind events compared to westerly, onshore winds (Whiteman et al. 2001, Zhong et al. 2001).

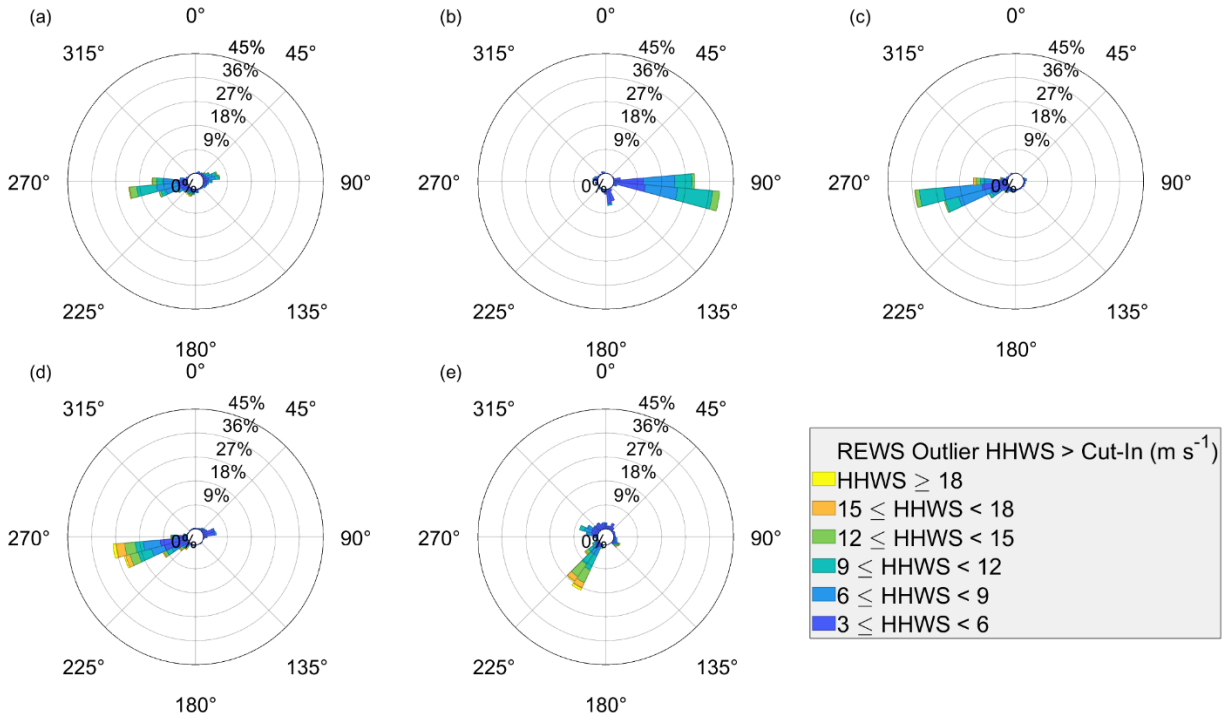

FIG. 17. Hub-height wind speed during WFIP2 *REWS* outlier events at (a) Gordon Ridge, (b) Troutdale, (c) Wasco, (d) Arlington, and (e) Vansycle Ridge. Wind speeds below cut-in speed have been removed.

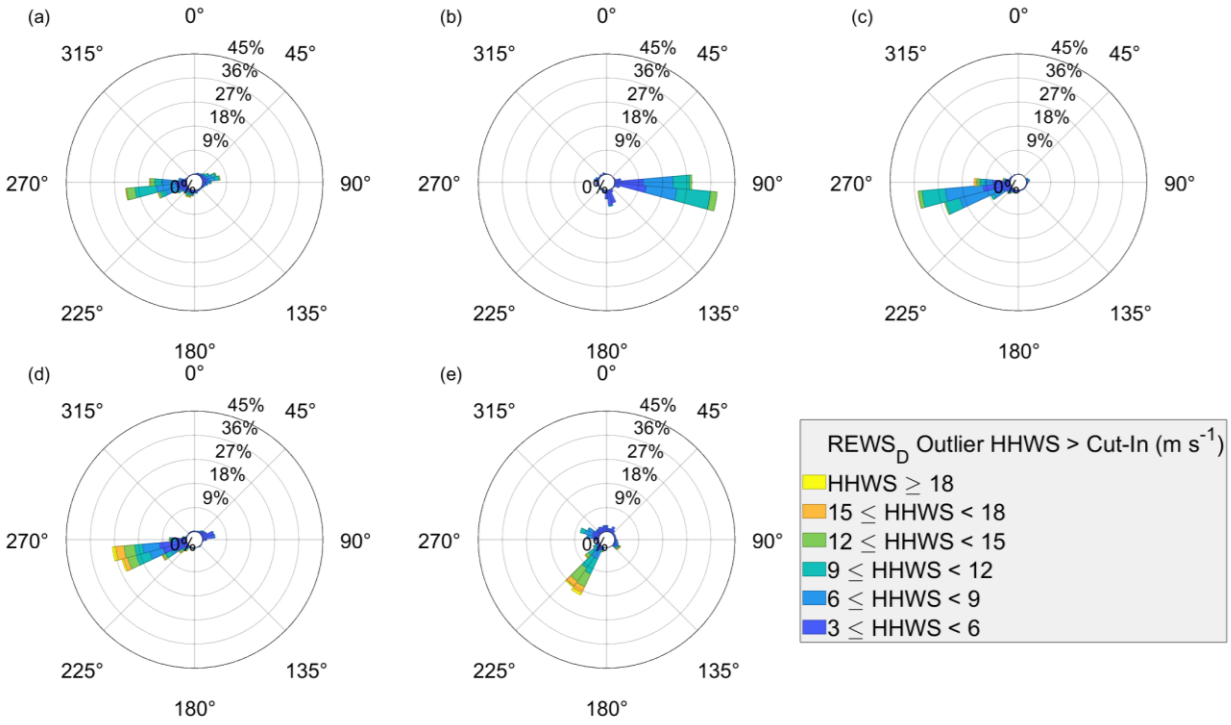

FIG. 18. Hub-height wind speed during WFIP2 $REWS_D$ outlier events at (a) Gordon Ridge, (b) Troutdale, (c) Wasco, (d) Arlington, and (e) Vansycle Ridge. Wind speeds below cut-in speed have been removed.

Directions differed for $REWS_{Alt}$ outlier events relative to the other REWS formulations. This translated into less frequent easterly events at Gordon Ridge. Vansycle Ridge recorded fewer southwesterly outlier events, and picked up more east-southeasterlies, perhaps related to a small subset of weaker downslope wind events which do not extend far enough from the base of the Blue Mountains to force strong winds at Pendleton, Walla Walla, or the surrounding region.

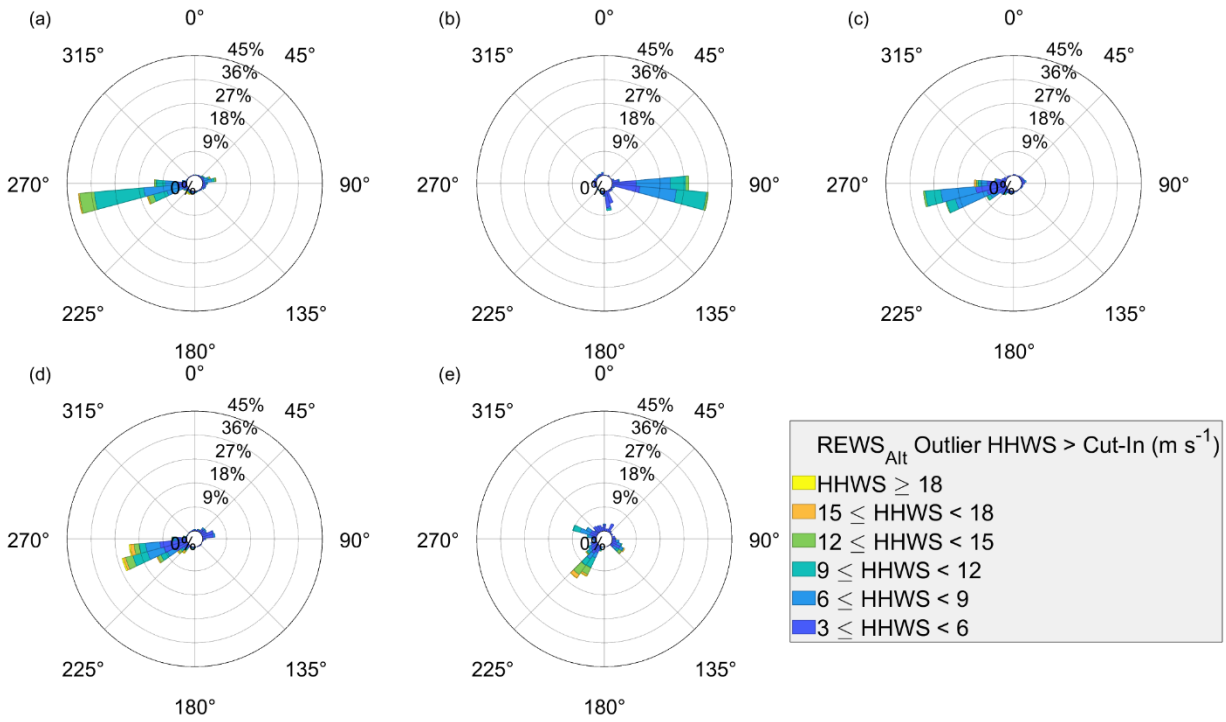

FIG. 19. HHWS during WFIP2 $REWS_{Alt}$ outlier events at (a) Gordon Ridge, (b) Troutdale, (c) Wasco, (d) Arlington, and (e) Vansycle Ridge. Wind speeds below cut-in speed have been removed.

5. Discussion and Conclusions

Profiling LiDAR data collected from five sites across Oregon during the WFIP2 field campaign were analyzed to determine if differences between HHWS and REWS existed during complex terrain. Statistical outliers (based on Tukey's method) were identified for times when HHWS and REWS differed, and outlier times were further classified into outlier events based on temporal persistence.

a. Key Findings

Most of the time (R^2 of 0.994 to 0.999) LiDAR-measured HHWS and calculated REWS (method-independent) were very closely matched.

Based on the Tukey method of identifying outliers in a dataset, there were times where HHWS and REWS differed. For locations within the Columbia Basin, a subset (16-32%) of outlier times occurred below turbine cut-in speed, thus limiting their importance for wind energy production. However, there were numerous identified events where winds were of a significant magnitude for wind energy production (i.e. above cut-in speed). These outliers were further grouped into events based on meeting criteria (defined by temporal persistence) outlined in the methods section.

Outlier events with HHWS faster than cut-in speed of 3 m s^{-1} frequently occurred during the morning and evening transition periods. During this period, the wind and temperature profiles of the planetary boundary layer undergo a transition from a well-mixed boundary layer (especially in the warm season) during the afternoon to a decoupled layer with more speed and direction shear across the lowest few hundred meters of the atmosphere, and thus across the rotor disk of wind turbines.

REWS and $REWS_D$ favored the morning and evening transition periods at Wasco and Arlington while ridge-top locations (Gordon Ridge and Vansycle Ridge) exhibited less diurnal preference for outlier events. This is likely due to their ridge-top location where the nocturnal stable boundary layer may be interrupted more readily by transient weather systems, especially during the winter months.

The inclusion of turbulence intensity in $REWS_{Alt}$ resulted in altered diurnal and seasonal tendencies for outlier events above cut-in speed when compared to *REWS* and $REWS_D$. Additionally, outlier events above cut-in speed were reduced in frequency for all sites.

Outlier events above cut-out speed (25 m s^{-1}) were limited and not quantified.

Diurnal and seasonal tendences of outlier events may be sensitive to the removal of winds below cut-in speed prior to classification.

For sites within the Columbia Basin, calculated AEP varied by 7% or less for all REWS methods when compared against AEP calculated from HHWS. Variations at Troutdale were larger, but deemed less important due to the lack of wind resources in the area. Clack et al. 2016 also determined that estimates depend on geographic location.

The inclusion of turbulence intensity led to higher AEP for all sites relative to the other REWS methods. This finding is consistent with Choukulkar et al. 2016. Moreover, for sites within the Columbia Basin, this resulted in AEP values that exceeded those calculated with HHWS.

Based on the calculated differences in annual energy production (AEP), companies could choose to do a cost-benefit analysis to determine whether siting additional instrumentation (such as LiDARs) would be worth the cost of installation and maintenance. Moreover, as HHWS and REWS are frequently interchangeable, the additional computing power required to perform calculations of REWS should be considered for modeling efforts.

This study can be used as a model for future observational studies in varying geographic areas of interest for wind energy production, though it should be noted that the complex terrain and prevailing synoptic pattern of the Columbia Basin may differ from other study areas, thus potentially yielding different results.

b. Future Work

Future work may include performing shape-based clustering analysis of wind speed and direction profiles for outlier events where REWS or HHWS are above cut-in speed. The methods described in Molina-Garcia et al., 2019 may facilitate classification of real-world speed and

direction profiles that are impactful for wind energy production. Moreover, shape-based clustering may aid in forecasting accurate profiles for predictable events such as wintertime cold pool episodes. Profiles during mountain-wave events may be more challenging to predict, but they still have a sizable impact on wind energy production as noted by Draxl et al., 2021

Additional future work may include a more robust analysis of a range of hub heights, including a comparison between the 80-m hub height that was examined in this study and a 100-m hub height that is more representative of newly installed turbines in the region.

Lastly, the removal of wind speeds below cut-in speed prior to the calculation of outlier times may lead to different results and will be studied in the future.

Acknowledgements

The author would like to thank his committee members, the University of Colorado Boulder's Department of Atmospheric and Oceanic Sciences (ATOC), and the Graduate School for their guidance and patience during his time as a graduate student.

References

2022: IEC 61400-12 Wind energy generation systems - Part 12: Power performance measurements of electricity producing wind turbines - Overview.

Abatzoglou, J. T., B. J. Hatchett, P. Fox-Hughes, A. Gershunov, and N. J. Nauslar, 2021: Global climatology of synoptically-forced downslope winds. *Intl Journal of Climatology*, **41**, 31–50, https://doi.org/10.1002/joc.6607.

Aitken, M. L., M. E. Rhodes, and J. K. Lundquist, 2012: Performance of a Wind-Profiling Lidar in the Region of Wind Turbine Rotor Disks. *Journal of Atmospheric and Oceanic Technology*, **29**, 347–355, https://doi.org/10.1175/JTECH-D-11-00033.1.

Akish, E., L. Bianco, I. V. Djalalova, J. M. Wilczak, J. B. Olson, J. Freedman, C. Finley, and J. Cline, 2019: Measuring the impact of additional instrumentation on the skill of numerical weather prediction models at forecasting wind ramp events during the first Wind Forecast Improvement Project (WFIP). *Wind Energy*, **22**, 1165–1174, https://doi.org/10.1002/we.2347.

Bardal, L. M., L. R. Sætran, and E. Wangsness, 2015: Performance Test of a 3MW Wind Turbine – Effects of Shear and Turbulence. *Energy Procedia*, **80**, 83–91, https://doi.org/10.1016/j.egypro.2015.11.410.

Bodini, N., J. K. Lundquist, R. Krishnamurthy, M. Pekour, and L. K. Berg, 2019: *Spatial and temporal variability of turbulence dissipation rate in complex terrain*. Dynamics/Field Measurements/Troposphere/Physics (physical properties and processes),.

Bossavy, A., R. Girard, and G. Kariniotakis, 2013: Forecasting ramps of wind power production with numerical weather prediction ensembles. *Wind Energy*, **16**, 51–63, https://doi.org/10.1002/we.526.

Choukulkar, A., Y. Pichugina, C. T. M. Clack, R. Calhoun, R. Banta, A. Brewer, and M. Hardesty, 2016: A new formulation for rotor equivalent wind speed for wind resource assessment and wind power forecasting: New formulation for equivalent wind speed. *Wind Energ.*, **19**, 1439–1452, https://doi.org/10.1002/we.1929.

Clack, C. T. M., A. Alexander, A. Choukulkar, and A. E. MacDonald, 2016: Demonstrating the effect of vertical and directional shear for resource mapping of wind power. *Wind Energ.*, **19**, 1687–1697, https://doi.org/10.1002/we.1944.

Dupont, E., R. Koppelaar, and H. Jeanmart, 2018: Global available wind energy with physical and energy return on investment constraints. Applied Energy, 209, 322–338, https://doi.org/10.1016/j.apenergy.2017.09.085.

Draxl, C., and Coauthors, 2021: Mountain waves can impact wind power generation. *Wind Energ. Sci.*, **6**, 45–60, https://doi.org/10.5194/wes-6-45-2021.

Golston, L., and Coauthors, 2019: Wind Power An Energy Technology Distillate from the

Andlinger Center for Energy and the Environment at Princeton University. https://acee.princeton.edu/wp-content/uploads/2019/04/AndlingerDistillate_Full2019_V10.pdf.

Hoen, B.D., Diffendorfer, J.E., Rand, J.T., Kramer, L.A., Garrity, C.P., and Hunt, H.E., 2018, United States Wind Turbine Database (ver 6.1, November 2023): U.S. Geological Survey, American Clean Power Association, and Lawrence Berkeley Laboratory data release, https://doi.org/10.5066/F7TX3DN0.

Iungo, G. V., Y.-T. Wu, and F. Porté-Agel, 2013: Field Measurements of Wind Turbine Wakes with Lidars. *Journal of Atmospheric and Oceanic Technology*, **30**, 274–287, https://doi.org/10.1175/JTECH-D-12-00051.1.

McCaffrey, K., and Coauthors, 2019: Identification and Characterization of Persistent Cold Pool Events from Temperature and Wind Profilers in the Columbia River Basin. *Journal of Applied Meteorology and Climatology*, **58**, 2533–2551, https://doi.org/10.1175/JAMC-D-19-0046.1.

Molina-Garcia, A., A. Fernandez-Guillamon, E. Gomez-Lazaro, A. Honrubia-Escribano, and M. C. Bueso, 2019: Vertical Wind Profile Characterization and Identification of Patterns Based on a Shape Clustering Algorithm. *IEEE Access*, **7**, 30890–30904, https://doi.org/10.1109/ACCESS.2019.2902242.

Olson, J. B., and Coauthors, 2019: Improving Wind Energy Forecasting through Numerical Weather Prediction Model Development. *Bulletin of the American Meteorological Society*, **100**, 2201–2220, https://doi.org/10.1175/BAMS-D-18-0040.1.

Pichugina, Y. L., and Coauthors, 2019: Spatial Variability of Winds and HRRR–NCEP Model Error Statistics at Three Doppler-Lidar Sites in the Wind-Energy Generation Region of the Columbia River Basin. *Journal of Applied Meteorology and Climatology*, **58**, 1633–1656, https://doi.org/10.1175/JAMC-D-18-0244.1.

Redfern, S., J. B. Olson, J. K. Lundquist, and C. T. M. Clack, 2019: Incorporation of the Rotor-Equivalent Wind Speed into the Weather Research and Forecasting Model's Wind Farm Parameterization. *Monthly Weather Review*, **147**, 1029–1046, https://doi.org/10.1175/MWR-D-18-0194.1.

Rhodes, M. E., and J. K. Lundquist, 2013: The Effect of Wind-Turbine Wakes on Summertime US Midwest Atmospheric Wind Profiles as Observed with Ground-Based Doppler Lidar. *Boundary-Layer Meteorol*, **149**, 85–103, https://doi.org/10.1007/s10546-013-9834-x.

Sanchez Gomez, M., and J. K. Lundquist, 2019: *The effect of wind direction shear on turbine performance in a wind farm in central Iowa*. Aerodynamics and hydrodynamics,.

Scheurich, F., P. B. Enevoldsen, H. N. Paulsen, K. K. Dickow, M. Fiedel, A. Loeven, and I. Antoniou, 2016: Improving the Accuracy of Wind Turbine Power Curve Validation by the Rotor Equivalent Wind Speed Concept. *J. Phys.: Conf. Ser.*, **753**, 072029, https://doi.org/10.1088/1742-6596/753/7/072029.

Schmitz, S., 2011: A WIND TURBINE Design and Analysis Tool. https://www.aero.psu.edu/Faculty_Staff/schmitz/XTurb/XTurb.html.

Seo, S., 2006: A Review and Comparison of Methods for Detecting Outliers in Univariate Data Sets. M.S. thesis, Graduate School of Public Health, University of Pittsburgh, 53 pp.

Sharp, J., and C. F. Mass, 2004: Columbia Gorge Gap Winds: Their Climatological Influence and Synoptic Evolution. Weather and Forecasting, 19, 970–992, https://doi.org/10.1175/826.1.

Slinger, C., and M. Harris, 2012: Introduction to continuous-wave Doppler lidar. https://breeze.colorado.edu/ftp/RSWE/Chris_Slinger.pdf.

Van Sark, W. G. J. H. M., H. C. Van Der Velde, J. P. Coelingh, and W. A. A. M. Bierbooms, 2019: Do we really need rotor equivalent wind speed? *Wind Energy*, **22**, 745–763, https://doi.org/10.1002/we.2319.

Vanderwende, B. J., and J. K. Lundquist, 2012: The modification of wind turbine performance by statistically distinct atmospheric regimes. *Environ. Res. Lett.*, **7**, 034035, https://doi.org/10.1088/1748-9326/7/3/034035.

de Vries, O., 1979: *Fluid Dynamic Aspects of Wind Energy Conversion*. National Aerospace Laboratory NLR,.

Wagner, R., I. Antoniou, S. M. Pedersen, M. S. Courtney, and H. E. Jørgensen, 2009: The influence of the wind speed profile on wind turbine performance measurements. *Wind Energ.*, **12**, 348–362, https://doi.org/10.1002/we.297.

Wagner, R., M. Courtney, J. Gottschall, and P. Lindelöw-Marsden, 2011: Accounting for the speed shear in wind turbine power performance measurement. *Wind Energy*, **14**, 993–1004, https://doi.org/10.1002/we.509.

Wagner, R., and Coauthors, 2014: Rotor equivalent wind speed for power curve measurement – comparative exercise for IEA Wind Annex 32. *J. Phys.: Conf. Ser.*, **524**, 012108, https://doi.org/10.1088/1742-6596/524/1/012108.

Wharton, S., J. F. Newman, G. Qualley, and W. O. Miller, 2015: Measuring turbine inflow with vertically-profiling lidar in complex terrain. *Journal of Wind Engineering and Industrial Aerodynamics*, **142**, 217–231, https://doi.org/10.1016/j.jweia.2015.03.023.

Whiteman, C. D., S. Zhong, W. J. Shaw, J. M. Hubbe, X. Bian, and J. Mittelstadt, 2001: Cold Pools in the Columbia Basin. Wea. Forecasting, 16, 432–447, https://doi.org/10.1175/1520-0434(2001)016<0432:CPITCB>2.0.CO;2.

Wiser, R., and Coauthors, 2023: *Land-Based Wind Market Report: 2023 Edition*. https://www.energy.gov/eere/wind/articles/land-based-wind-market-report-2023-edition.

Zhong, S., C. D. Whiteman, X. Bian, W. J. Shaw, and J. M. Hubbe, 2001: Meteorological

Processes Affecting the Evolution of a Wintertime Cold Air Pool in the Columbia Basin. Mon. Wea. Rev., 129, 2600–2613, https://doi.org/10.1175/1520-0493(2001)129<2600:MPATEO>2.0.CO;2.

Appendix

a. Summary for the Wind Energy Industry

As wind turbines increase in size, the potential for greater differences in wind speed and direction across the turbine's rotor disk also increases. If these changes in wind speed and direction across the rotor disk are large, the assumption that the wind speed and direction at a wind turbine's hub height are representative across the turbine's rotor disk may not be true. Moreover, this may lead to errors in the estimation of power produced by the turbine. Therefore, an alternative to hub-height wind speed (HHWS) is a rotor-equivalent wind speed (REWS). This REWS quantifies the momentum entering the wind turbine rotor disk by averaging the weighted wind speed over the disk's swept area. REWS theoretically offers a more accurate wind speed estimate for power production than simply using the HHWS.

This study takes an observational dataset of LiDAR-measured wind from the Second Wind Forecast Improvement Project (WFIP2) and examines the differences between HHWS and three variants of REWS. The resulting distributions of HHWS and REWS are used in conjunction with the theoretical power curve of a wind turbine of similar specifications to existing turbines in the region to calculate annual energy production (AEP).

Differences between HHWS and REWS are generally small, as illustrated in Figure A1.

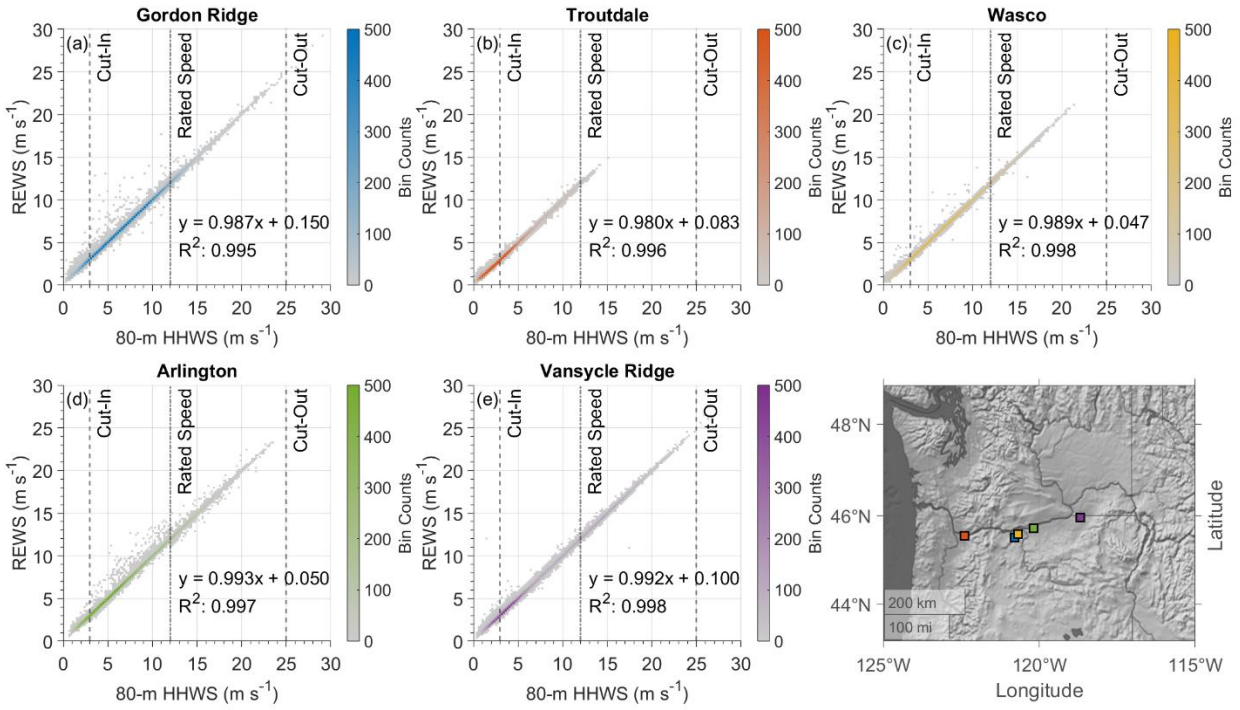

FIG. A1. Binned scatter plot of REWS vs 80-m HHWS during WFIP2 at (a) Gordon Ridge, (b) Troutdale, (c) Wasco, (d) Arlington, and (e) Vansycle Ridge. Linear regression equations and R^2 values are displayed in the lower right corner for each site. A site map is provided in the lower right corner.

Vertical profiles of wind speed and wind direction during sample outlier events are shown in Figures A2 and A3.

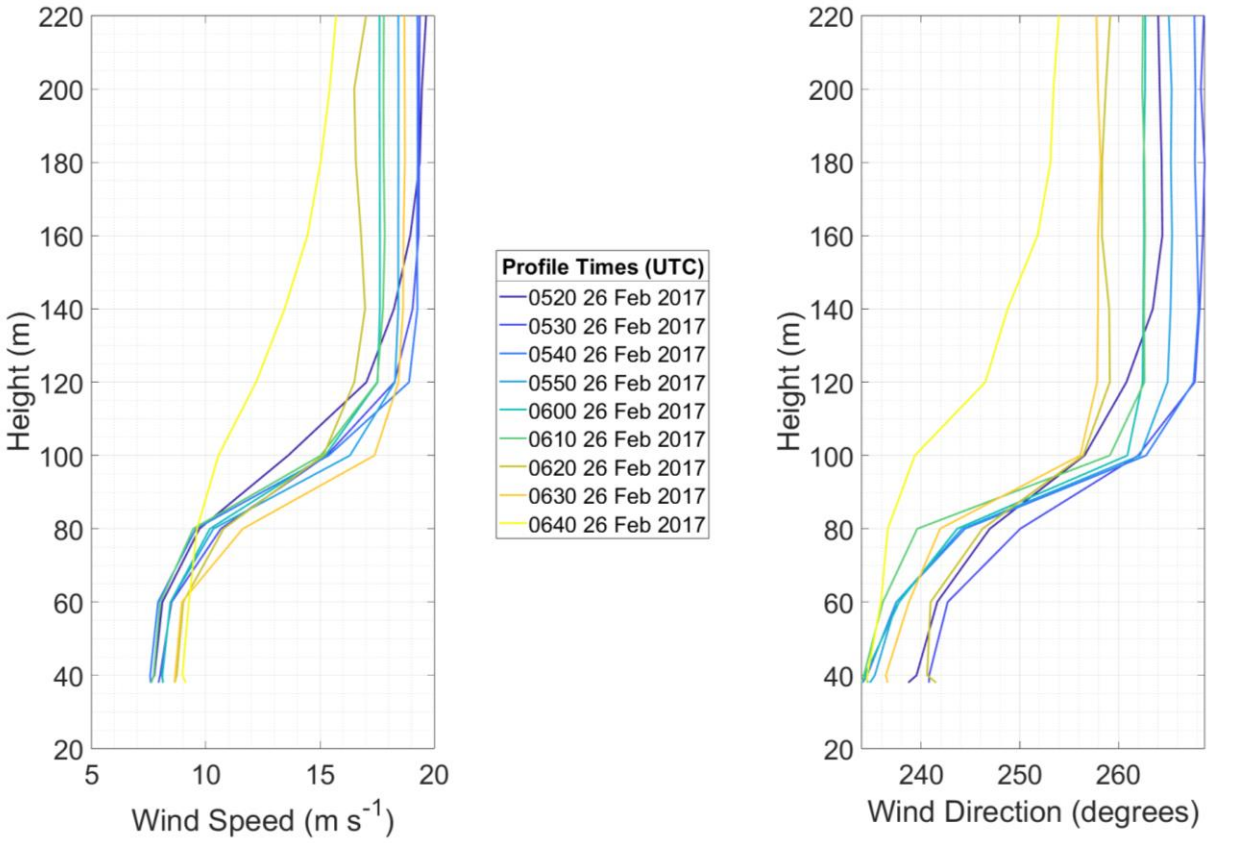

FIG. A2. Wind speed and direction profiles at Arlington during the 26 February 2017 outlier event. Times are in UTC.

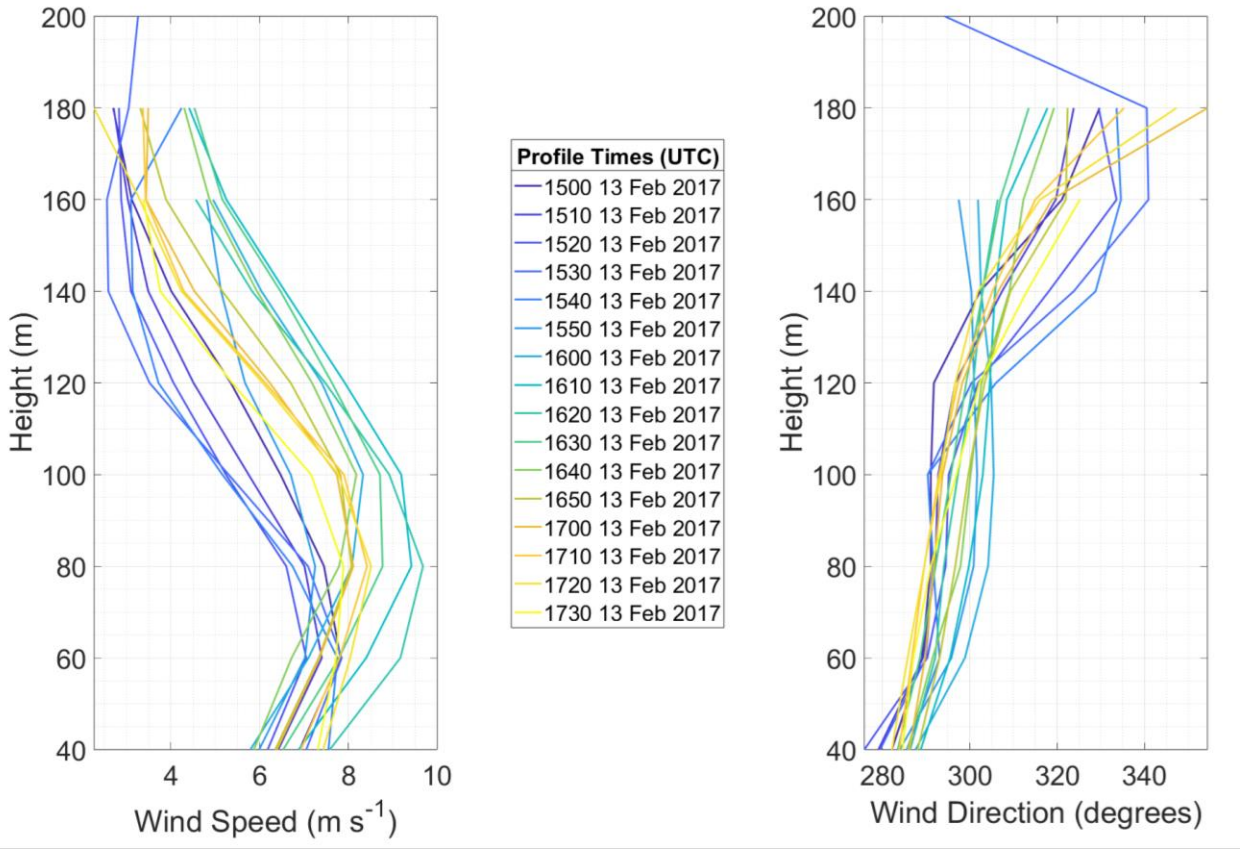

Fig. A3. Wind speed and direction profiles at Vansycle Ridge during the 13 February 2017 outlier event. This event was studied by McCaffrey et al. 2019. Times are in UTC.

The differences between AEP calculated from the REWS distributions relative to the HHWS distribution are small, ranging from -1.1 percent to +7 percent.

In regions of complex terrain, REWS may provide a more accurate wind resource assessment, but the cost of deploying measurements that span the turbine rotor (rather than just measuring at hub height) must also be considered.